

CHARACTERIZATION AND IMAGING OF SINGLE  
LAYERED MATERIALS BY THE LAMB WAVE LENS

A THESIS  
SUBMITTED TO THE DEPARTMENT OF ELECTRICAL AND  
ELECTRONICS ENGINEERING  
AND THE INSTITUTE OF ENGINEERING AND SCIENCES  
OF BILKENT UNIVERSITY  
IN PARTIAL FULFILLMENT OF THE REQUIREMENTS  
FOR THE DEGREE OF  
MASTER OF SCIENCE

By  
S. Ayhan ÖZGÜR

JULY, 1991

TA  
417.23  
.D44  
1991

CHARACTERIZATION AND IMAGING OF SINGLE  
LAYERED MATERIALS BY THE LAMB WAVE LENS

A THESIS

SUBMITTED TO THE DEPARTMENT OF ELECTRICAL AND  
ELECTRONICS ENGINEERING

AND THE INSTITUTE OF ENGINEERING AND SCIENCES  
OF BILKENT UNIVERSITY

IN PARTIAL FULFILLMENT OF THE REQUIREMENTS  
FOR THE DEGREE OF  
MASTER OF SCIENCE

By

F. Levent Değertekin

July 1991

*F. Levent Değertekin*  

---

*tarafından hazırlanmıştır.*

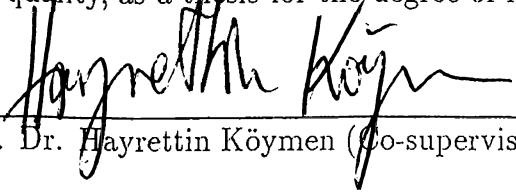
7A  
417.23  
-D44  
1031

B-8903

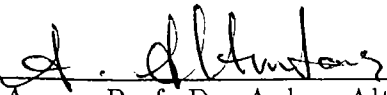
I certify that I have read this thesis and that in my opinion it is fully adequate, in scope and in quality, as a thesis for the degree of Master of Science.

  
\_\_\_\_\_  
Prof. Dr. Abdullah Atalar(Supervisor)


I certify that I have read this thesis and that in my opinion it is fully adequate, in scope and in quality, as a thesis for the degree of Master of Science.

  
\_\_\_\_\_  
Prof. Dr. Hayrettin Köymen (Co-supervisor)


I certify that I have read this thesis and that in my opinion it is fully adequate, in scope and in quality, as a thesis for the degree of Master of Science.

  
\_\_\_\_\_  
Assoc. Prof. Dr. Ayhan Altıntaş

I certify that I have read this thesis and that in my opinion it is fully adequate, in scope and in quality, as a thesis for the degree of Master of Science.

  
\_\_\_\_\_  
Assoc. Prof. Dr. Levent Onural

Approved for the Institute of Engineering and Sciences:

  
\_\_\_\_\_  
Prof. Dr. Mehmet Baray  
Director of Institute of Engineering and Sciences

# ABSTRACT

## CHARACTERIZATION AND IMAGING OF SINGLE LAYERED MATERIALS BY THE LAMB WAVE LENS

F. Levent Değertekin

M.S. in Electrical and Electronics Engineering

Supervisors: Prof. Dr. Abdullah Atalar  
and Prof. Dr. Hayrettin Köymen

July 1991

The Lamb wave lens, which was introduced earlier as a new kind of lens for scanning acoustic microscope, is analyzed theoretically. A simulation program capable of handling single layered materials with different material parameters and bonding conditions is developed. The validity of theory is investigated by comparing the simulation results with the experimental ones for specially prepared samples. Parameter sensitivity of  $V(f)$  curves are used to test the characterization ability of the lens in layered materials. Subsurface imaging ability of the Lamb wave lens is also investigated by forming amplitude and peak frequency images of some samples.

Keywords: Lamb wave lens, scanning acoustic microscope, layered material characterization,  $V(f)$  curves.

## ÖZET

### TEK KATMANLI MALZEMELERİN LAMB DALGASI MERCEĞİ İLE TANIMLANMASI VE GÖRÜNTÜLENMESİ

F. Levent Değertekin

Elektrik ve Elektronik Mühendisliği Bölümü Yüksek Lisans

Tez Yöneticileri: Prof. Dr. Abdullah Atalar

ve Prof. Dr. Hayrettin Köymen

Temmuz 1991

Taramalı akustik mikroskop için yeni bir tür mercek olarak daha önce önerilmiş olan Lamb dalgası merceğinin kuramsal analizi yapılmıştır. Değişik parametre ve bağlantı özelliği olan tek katmanlı malzemeler için bir benzetim programı geliştirilmiştir. Kuramın geçerliliği, özel olarak yapılan örnek malzemelerde deneysel ve benzetim sonuçları karşılaştırılarak incelenmiştir.  $V(f)$  eğrilerinin parametre duyarlılığı incelenerek merceğin katmanlı malzeme tanımlama yeteneği araştırılmıştır. Lamb dalgası merceğinin yüzeyaltı görüntüleme yeteneği ise bazı örnek malzemelerin genlik ve tepe frekansı görüntüleri alınarak incelenmiştir.

Anahtar sözcükler: Lamb dalgası merceği, taramalı akustik mikroskop, katmanlı malzeme tanımlanması,  $V(f)$  eğrileri.

## ACKNOWLEDGMENT

I am grateful to Prof. Dr. Abdullah Atalar and Prof. Dr. Hayrettin Köymen for their supervision, guidance, suggestions and patience throughout the development of this thesis.

I would like to thank Tuna Karayel and Fatih Erden for their early work on the simulation program and Prof. Dr. Levent Toppare and Sakıp Doğan from METU for their helps during the preparation of the sample materials. I am also grateful to Mustafa Karaman and Satılmış Topçu for their continuous encouragement during all the stages of this thesis.

# Contents

<b>1</b>	<b>Introduction</b>	<b>1</b>
<b>2</b>	<b>Theory</b>	<b>3</b>
2.1	Excitation of leaky waves . . . . .	3
2.2	The Lamb wave lens . . . . .	5
2.3	Response of the Lamb wave lens . . . . .	11
2.4	$V(f)$ Curves . . . . .	13
<b>3</b>	<b>Simulation</b>	<b>17</b>
3.1	Calculation of the Reflection Coefficient . . . . .	17
3.2	Calculation of $V(f)$ Curves	20
<b>4</b>	<b>Experimentation</b>	<b>22</b>
4.1	The Lens . . . . .	22
4.2	Electronic Setup . . . . .	23
4.3	Imaging Setup . . . . .	24
4.4	The Samples . . . . .	25
<b>5</b>	<b>Results</b>	<b>26</b>
5.1	$V(f)$ Results	26



<i>CONTENTS</i>	vii
5.2 Images . . . . .	28
<b>6 Conclusion</b>	<b>32</b>
<b>A Calculation of the curvature matrix of a cone</b>	<b>34</b>
<b>B Material Constants Used in Simulations</b>	<b>36</b>

## List of Figures

2.1	The phase velocity of the leaky modes as a function of frequency thickness product for copper layer on steel halfspace.	4
2.2	The schematic diagram of nonspecular reflection at a liquid - layered solid material interface. Dashed lines indicate specular reflection, the reflected field is concentrated in the shaded region, $\Delta_S$ is the Schoch displacement.	4
2.3	Magnitude (dotted) and phase (solid) of the reflection coefficient at water-0.6 mm copper layered aluminum interface as a function of incidence angle at $f = 7$ MHz. . . . .	5
2.4	Geometry of the Lamb wave lens. . . . .	6
2.5	Geometry for refraction at $Q_R$ . The plane of incidence is the plane of the paper. . . . .	7
2.6	The geometry of the lens and the refracted conical wavefront.	8
2.7	Incident and reflected spatial field distributions on the surface of the sample with 0.5 mm copper layer on steel substrate.	9
2.8	$R(f)$ curve at an incidence angle of 35.8 degrees at water- 0.5 mm copper layered steel interface. . . . .	10
2.9	Geometry for the Ray Theory. . . . .	12
2.10	The variation of output signal amplitude as a function of lens-sample distance for two different frequency values for the sample in Figure 2.8. . . . .	14
2.11	The $V(f)$ curve of the sample in Figure 2.8. . . . .	15

2.12	Calculated $V(f)$ curves for a good bond, slippery bond and delamination at the interface of 6 $\mu\text{m}$ aluminum layer on silicon substrate.	16
3.1	Geometry and coordinate system for the layered material.	18
4.1	Functional block diagram of the experimental setup. . . . .	23
5.1	Calculated and measured $V(f)$ curves for a good bond and slippery bond. The sample is 0.6 mm copper layered steel substrate.	27
5.2	Calculated and measured $V(f)$ curves for a good bond and a delamination. The sample is 0.5 mm copper layered steel substrate.	28
5.3	Calculated $V(f)$ curves for unperturbed, and perturbed layer parameters in case of good bond. The density, $\rho$ , and shear constant, $c_{44}$ , of the layer are increased 5 %. . . . .	29
5.4	Calculated percentage shift in $V(f)$ as a function of percentage changes in layer $\rho$ and $c_{44}$ . . . . .	30
5.5	Calculated $V(f)$ curves for good bond, slippery bond and delamination for 40 $\mu\text{m}$ chromium layer on steel substrate.	30
5.6	Amplitude image of the sample with 0.6 mm Cu layer on steel at 7.9 MHz. . . . .	31
5.7	Peak frequency image of the same region in Figure 5.6. . . . .	31
A.1	Geometry and the coordinate system of the cone.	35

# Chapter 1

## Introduction

Nearly all forms of energy, including electromagnetic, acoustic, nuclear and thermal, have been used to nondestructively investigate the structure and properties of materials [1]. Acoustic energy is one of the most widely used of these forms because

- it can be inexpensively generated and detected,
- it can propagate into the interior of many structures with tolerable attenuation,
- the return signals carry sufficient information to characterize the materials and their defects.

Of these facts, the penetration ability provides acoustic methods a superiority above optical ones through subsurface imaging of optically opaque materials.

Layered materials are becoming increasingly important in many industrial products, because they enhance the quality of the product by increasing its resistance to outside effects such as corrosion. Depending on the application, the number of layers can change as well as the layer materials. Different types of defects (adhesive, cohesive), which lower the quality of material, can be induced during the production or usage of the layered materials. Adhesive defects, especially, can not be sensed by optical means. In such cases, acoustic methods appear as an effective tool for characterization and imaging of layered materials.

Scanning acoustic microscope (SAM) [2] is one of the most widely used acoustic tools in materials study. The spherical lens of SAM insonifies the

material by bulk waves at a continuum of incidence angles exciting all possible modes such as Rayleigh surface waves, Lamb waves etc., in addition to the bulk modes. As a result, the response of SAM is formed by the interference of specularly reflected waves with the reflected components caused by the other modes [3]. The  $V(Z)$  curve, obtained by recording this interference pattern as a function of the distance between the lens and material, has been shown to be a method for material characterization [4]. Using this method, SAM can characterize materials quantitatively with ability to measure adhesion properties, elastic constants, plastic deformations and piezoelectric performance. However, especially the SAM images of layered materials are very difficult to interpret because of the simultaneous excitation of all the modes that a layered material can support.

The Lamb wave lens, introduced earlier [5], was proposed to solve the multimode excitation problem of SAM in layered materials, by exciting a single possible mode at a time, since it insonifies the material with conical waves at a fixed incidence angle. When it is used as the lens of an acoustic microscope, the obtained subsurface images of layered materials are easy to interpret due to presence of a single mode. Since these modes are dispersive, it is possible to selectively excite the leaky modes by matching the fixed incidence angle with the critical angle of the mode at a particular frequency. If the return signal amplitude is recorded as a function of frequency, one obtains a unique  $V(f)$  curve which is highly dependent on elastic parameters of the layered material and quality of bonding at the interface [6]. The information contained in  $V(f)$  curves can also be used to form images revealing the spatial variation of the elastic parameters and bond quality of the material [7].

In this study, the Lamb wave lens is analyzed theoretically, a simulation program is developed to simulate the response of the Lamb wave lens to single layered materials with different parameters and bonding conditions at the interface and the validity of theory is investigated by performing  $V(f)$  measurements on some specially prepared samples. Amplitude and peak frequency images of the samples are formed to investigate the subsurface imaging ability of the Lamb wave lens.

In Chapter 2, the theoretical basis of the Lamb wave lens is investigated and its response is derived. Also, formation of the  $V(f)$  curves is explained. In Chapter 3, the simulation program is described in detail. The experimental setup used for  $V(f)$  measurements and imaging is presented in Chapter 4. The experimental and simulation results are given and compared with each other in Chapter 5. Finally, in Chapter 6, the conclusions are discussed.

## Chapter 2

### Theory

#### 2.1 Excitation of leaky waves

It is known that Rayleigh wave can be excited in a planar solid halfspace immersed in a liquid medium by acoustic wave insonification at a critical angle. If a thin layer is coated on top of such a solid halfspace, a new propagation medium emerges for many different modes such as Rayleigh-like and generalized Lamb wave modes [8].

The Rayleigh-like waves are confined to the surface and extend to depths of about one wavelength. The generalized Lamb waves behave like Lamb waves in plates [9]. All these modes are dispersive, their velocities change with frequency and thickness. This property can be seen in the velocity dispersion curves in Figure 2.1. As expected, the Rayleigh-like mode has a velocity equal to the Rayleigh wave velocity of the halfspace if there is no layer, and as the layer thickness increases, it approaches to the Rayleigh velocity of the layer material. Since the generalized Lamb wave modes are mostly of shear nature, their dispersion is limited between the shear wave velocities of the layer and of the halfspace.

If the layered material is immersed in a liquid medium and insonified by a bounded acoustic wave, it is seen that the reflected wave is like in Figure 2.2. The important features of the reflected field are the shift and the trailing field in the lateral direction in contrast to the geometrical specular reflection [10]. Since the acoustic wave is incident at a critical angle, a particular mode is excited. The mode begins to reradiate back to the liquid medium as soon as it is excited, in other words, some energy of the mode leaks back to the liquid medium causing the mode to be known as a *leaky wave mode* [11]. The lateral

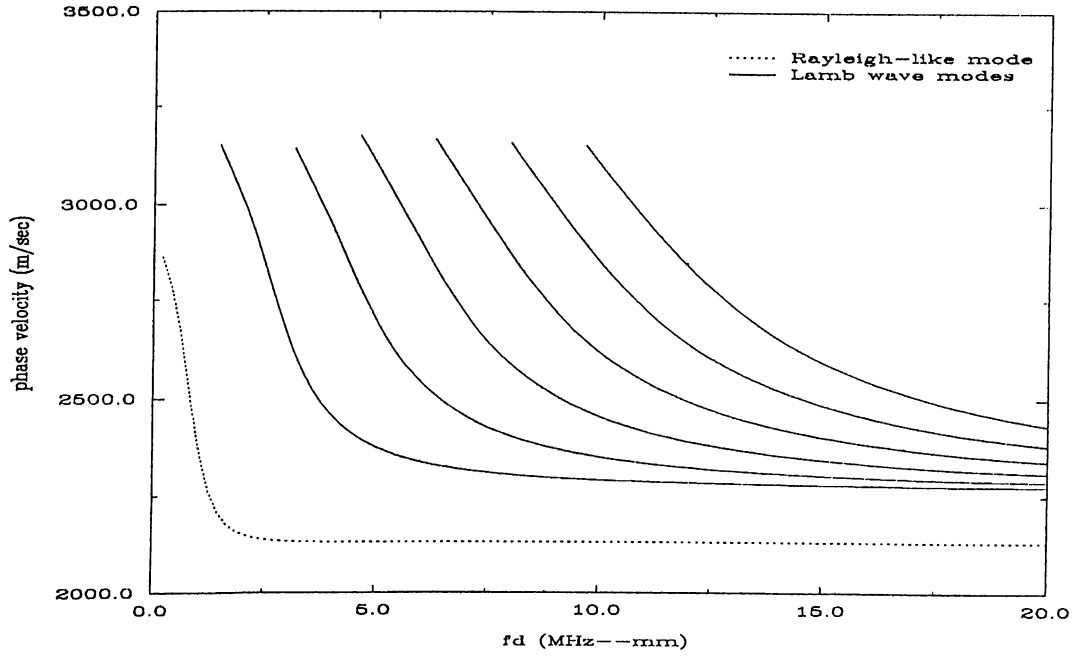


Figure 2.1: The phase velocity of the leaky modes as a function of frequency thickness product for copper layer on steel halfspace.

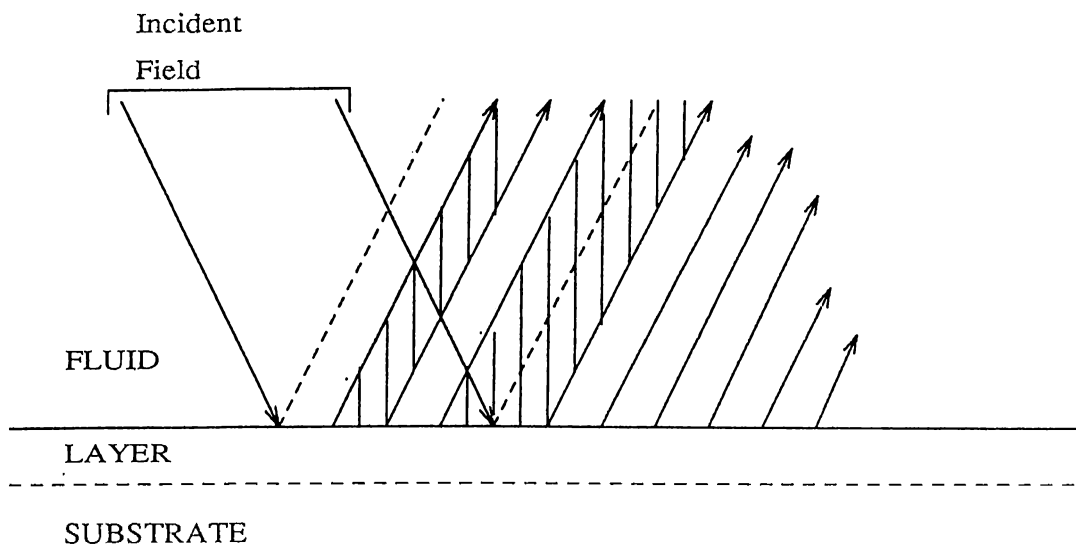


Figure 2.2: The schematic diagram of nonspecular reflection at a liquid - layered solid material interface. Dashed lines indicate specular reflection, the reflected field is concentrated in the shaded region.

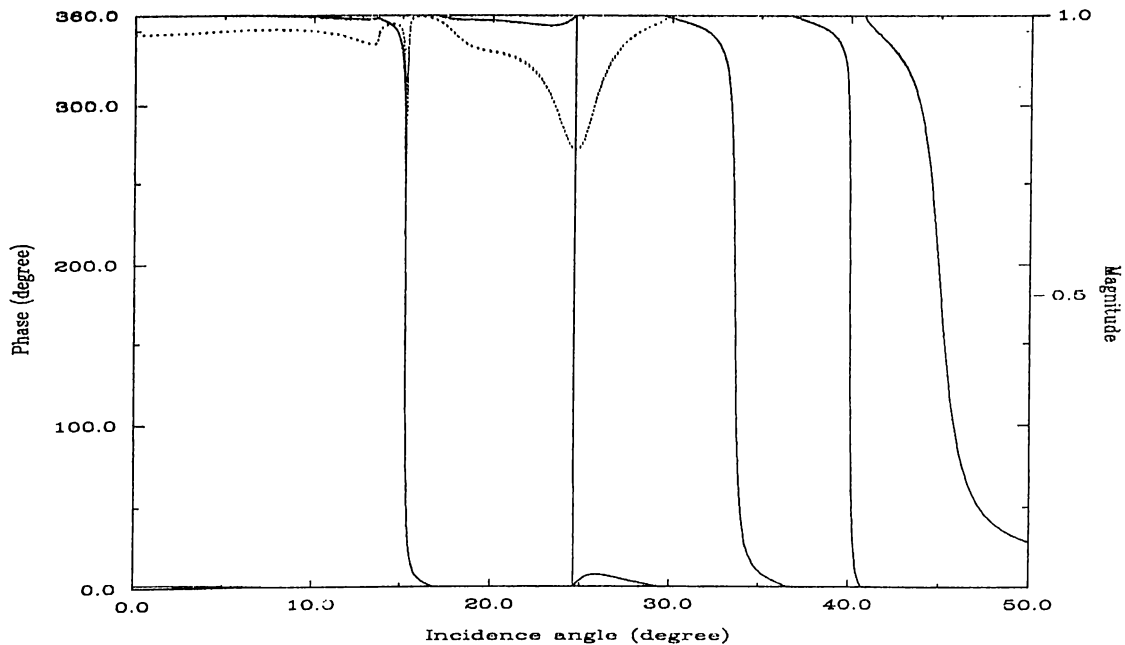


Figure 2.3: Magnitude (dotted) and phase (solid) of the reflection coefficient at water-0.6 mm copper layered aluminum interface as a function of incidence angle at  $f = 7$  MHz.

shift can be related to the Schoch displacement,  $\Delta_S$ , and it depends on the material specific space leak rate of the mode. The null region occurs as the result of the interference of the specularly reflected field with the nonspecular component. If the angle of incidence is not a critical angle, the reflected field has no such features, it has only the specular component.

The excitation of the leaky waves reveal themselves in the plane wave reflection coefficient as sharp phase transitions at the critical angles [12]. In Figure 2.3, the magnitude and phase of reflection coefficient at water - copper layered aluminum interface is plotted as a function of incidence angle at a fixed frequency. The sharp transitions in phase indicate mode excitations. One can use this graph to excite leaky modes in the layered material.

## 2.2 The Lamb wave lens

Leaky wave modes can be excited in a layered solid by acoustic wave insonification at an appropriate frequency and incidence angle in a liquid medium. This can be achieved easily and efficiently by using a wedge transducer [13], but it is not suitable for imaging because of its poor resolution. For high resolution



focusing is necessary. A method of focusing surface waves is to use conical waves incident on the solid at a critical angle. Conical waves can be generated by using a conical transducer or refraction or reflection from a suitable surface [14][15]. The Lamb wave lens seen in Figure 2.4 utilizes the refraction approach [5].

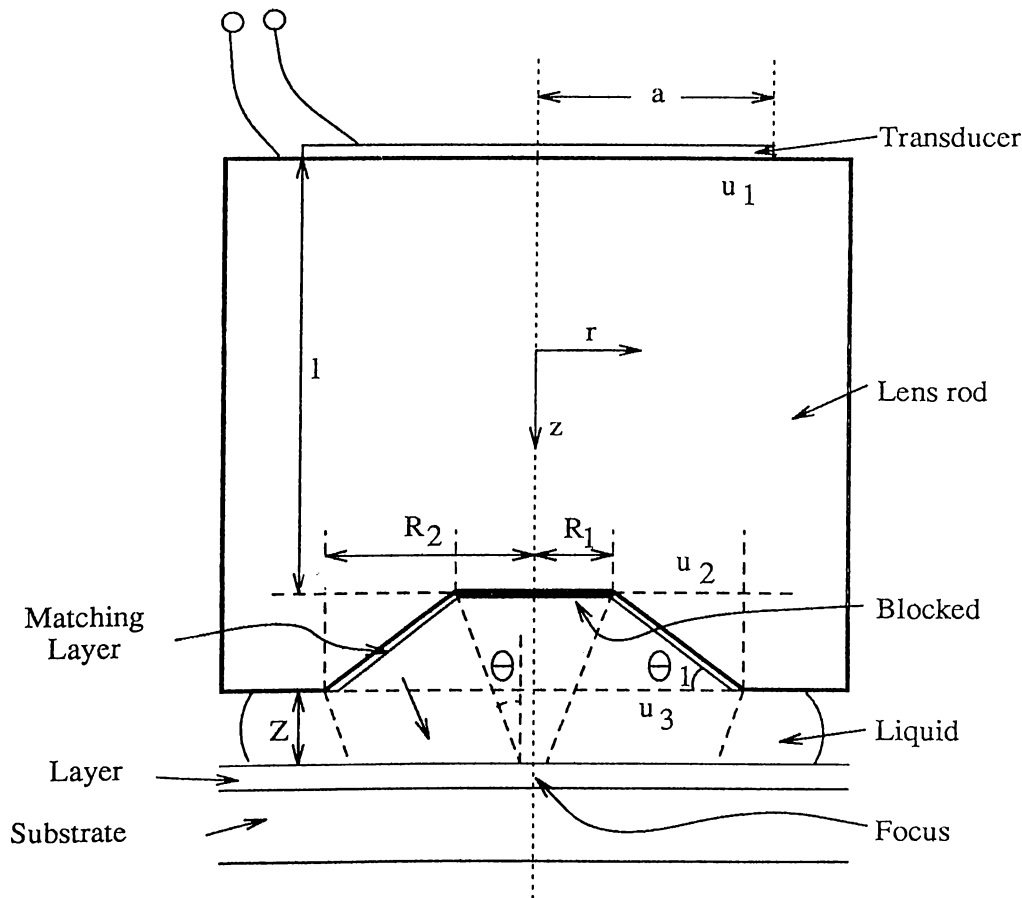


Figure 2.4: Geometry of the Lamb wave lens.

In this geometry, the acoustic waves generated by the transducer are refracted from the conical recess and form a conical wavefront incident on the layered material. Conical wavefront generation can be shown using the differential geometrical approach in [16]. Using the ray fixed coordinate system, the refraction process can be modeled as in Figure 2.5.

In the figure,  $\mathbf{n}$  is the unit normal vector and  $\mathbf{u}_1$  and  $\mathbf{u}_2$  are the principal direction vectors of the conical recess surface at  $Q_R$ ,  $\mathbf{x}_1$  and  $\mathbf{x}_2$  are the principal direction vectors of the incident wavefront. Since we assume plane wave incidence, we can freely choose  $\mathbf{x}_2 = \mathbf{u}_2$ . The primed quantities denote the corresponding quantities for the refracted ray. Then, using the approach in



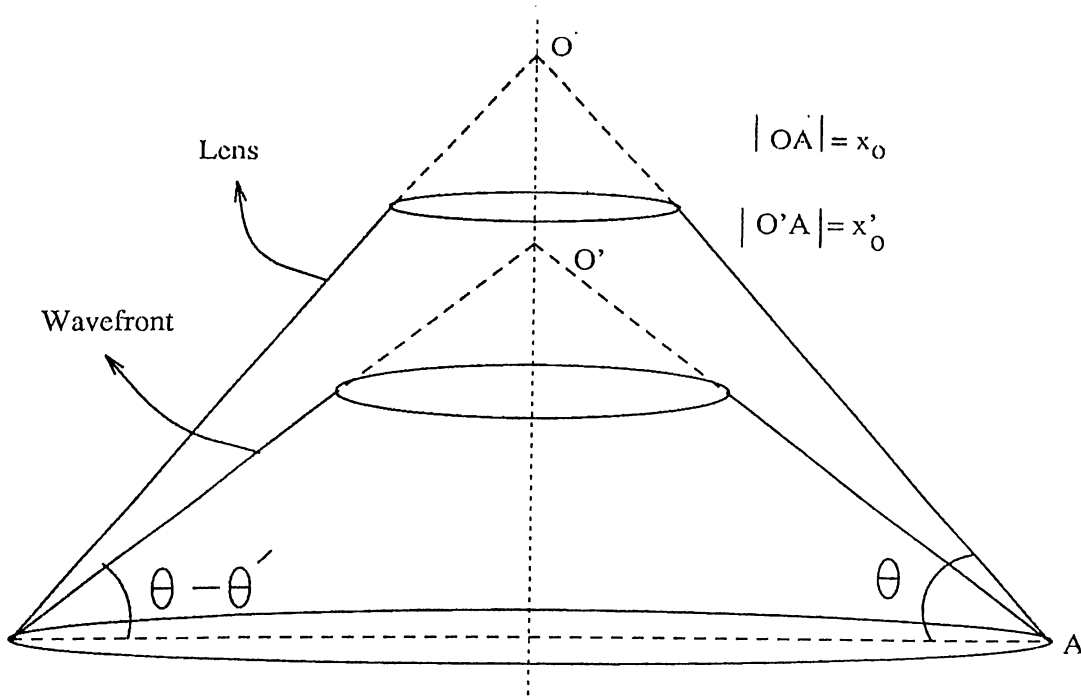


Figure 2.6: The geometry of the lens and the refracted conical wavefront.

$$\mathbf{C} = \begin{bmatrix} 0 & 0 \\ 0 & \frac{-4 \sin^2 \theta}{x_0 \sin 2\theta} \end{bmatrix} \quad (2.5)$$

Then using Eq. 2.4 the curvature matrix of the refracted wavefront is written as

$$\mathbf{Q}' = \left( \cos \theta' - \frac{k}{k'} \cos \theta \right) \begin{bmatrix} 0 & 0 \\ 0 & \frac{-4 \sin^2 \theta}{x_0 \sin 2\theta} \end{bmatrix} \quad (2.6)$$

Referring to Figure 2.6, the cone drawn for the refracted wavefront has  $\alpha' = 90 - (\theta - \theta')$  and  $x'_0 = x_0 \cos \theta / \cos(\theta - \theta')$ . Also from Snell's law we have  $\cos \theta' - \frac{k}{k'} \cos \theta = \sin(\theta - \theta') / \sin \theta$ . Substituting these in Eq. 2.6 we get the result as

$$\mathbf{Q}' = \begin{bmatrix} 0 & 0 \\ 0 & \frac{-4 \sin^2(\theta - \theta')}{x'_0 \sin 2(\theta - \theta')} \end{bmatrix} \quad (2.7)$$

Realizing that  $\mathbf{Q}'$  is the curvature matrix of the lower cone in Figure 2.6 with respect to the principal directions  $\mathbf{x}'_1$  and  $\mathbf{x}'_2$ , we see that the refracted wavefront is conical and has the shape seen in Figure 2.6. As a result we conclude that the Lamb wave lens transforms the incident plane wave to a conical wave with incidence angle  $\theta - \theta'$  and curvature matrix  $\mathbf{Q}'$ .

The angle of incidence of the conical waves can be adjusted by changing

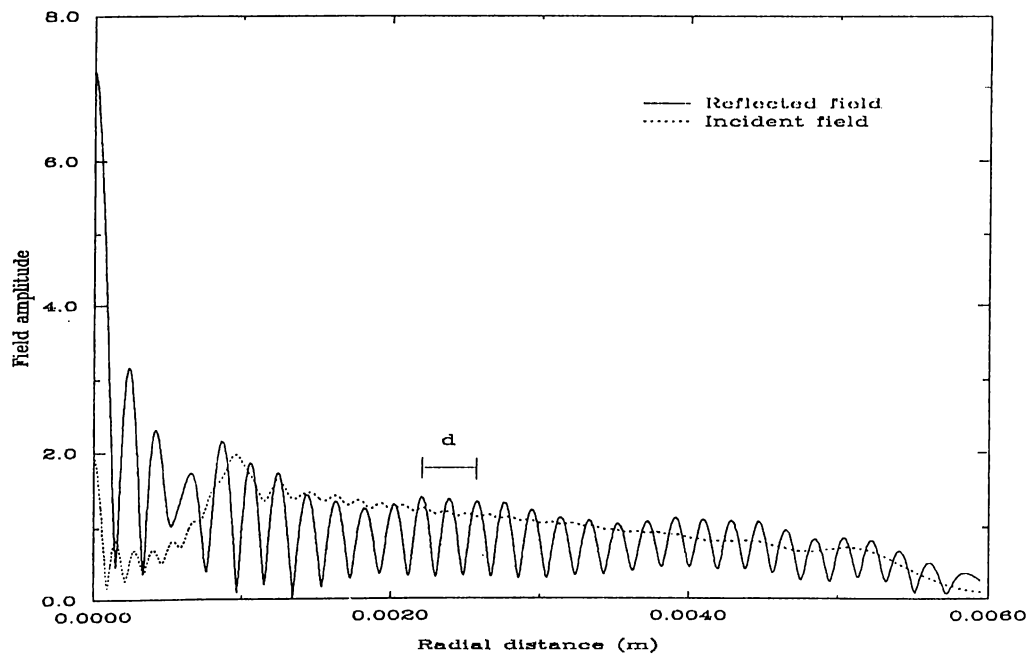


Figure 2.7: Incident and reflected spatial field distributions on the surface of the sample with 0.5 mm copper layer on steel substrate.

the angle of the refracting cone and taking Snell's law into consideration at the lens material-liquid interface. Using the dispersion curves, this angle can be chosen to match a critical angle. If the waves are incident at a critical angle, an evanescent Lamb wave is excited in the material. The Lamb wave lens detects the leaky waves with approximately 30% efficiency. This low efficiency results from the fact that most of the reflected field is blocked by the central part and some of the field leaks beyond the lens aperture.

The leaky waves converge in the material and focus at the point where the cone axis intersects the material plane. This focusing can be seen in Figure 2.7 in which the calculated incident and reflected field distributions on the layered material surface are plotted. The calculation is done at a frequency where a Lamb wave mode is excited. The distance between the ripples in the reflected field,  $d$ , satisfies the relation  $d = \lambda_w / \sin \theta$ , where  $\lambda_w$  is the wavelength in water at excitation frequency and  $\theta$  is the incidence angle. This relation shows that the reflected field pattern is the result of the interference between the leaky wave components excited from opposite sides of the lens, leaking into the liquid at the same angle  $\theta$ . If the leaky wave is not excited, the reflected field is nearly same as the incident field and the focusing effect is not seen.

The focused waves then diverge from the focus and leak back to the liquid at the same critical angle. After refraction from the conical surface, the waves

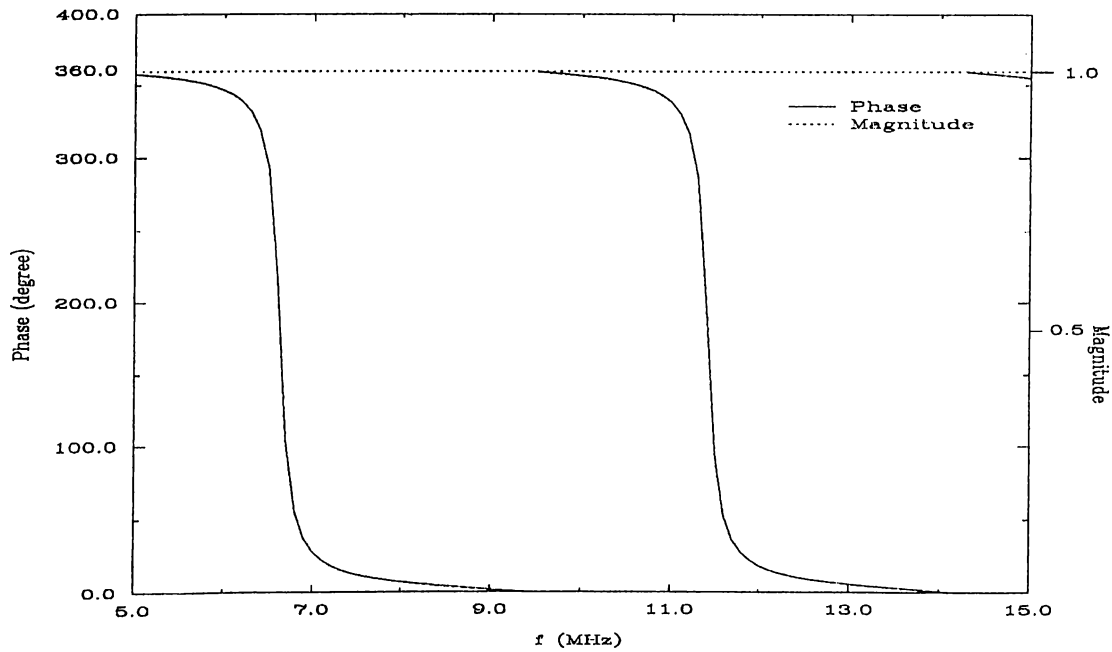


Figure 2.8:  $R(f)$  curve at an incidence angle of 35.8 degrees at water-0.5 mm copper layered steel interface.

are detected by the transducer. To prevent detection of the specularly reflected waves, the distance between the lens and the material,  $Z$ , should satisfy the condition  $Z < (R_1 / \tan \theta - (R_2 - R_1) \tan \theta_1)$ .

Since the leaky waves are dispersive, the fixed incidence angle of the lens can be made equal to a critical angle of a Lamb wave mode by adjusting the excitation frequency. By choosing the frequency properly, the modes can be excited in a selective manner. In Figure 2.8, the variation of the reflection coefficient at a fixed incidence angle as a function of frequency,  $R(f)$  curve, is plotted for a copper layered steel substrate. The phase transitions indicate mode excitations, hence show that desired modes can be excited by adjusting the frequency.

In the design of the Lamb wave lens, some points must be taken into consideration. The cone angle should be chosen using the dispersion curves of the layered materials of interest. The aperture width must be decided properly by considering the slope of the phase transitions in the reflection coefficient, hence the Schoch displacement. The transducer size and the lens rod length must be chosen to minimize the diffraction loss and the interference from the spurious pulses. The effective width of the conical surface must be large enough to have a narrow angular spectrum around the incidence angle. The effective width can be defined as the portion of the conical surface that is illuminated by the

transducer at the right incidence angle. If the angular spectrum is wide, i.e. there are waves incident at angles different from the desired angle, the excitation frequencies can deviate from the calculated values. The transducer must have a wide bandwidth in order to have a frequency scan. A matching layer should be deposited on the conical surface to decrease mismatch loss.

### 2.3 Response of the Lamb wave lens

The electrical return signal at the transducer terminals can be found by evaluating the voltage integral formula [17]. The formula gives the output voltage at the transducer terminals in terms of the scalar wave potential only, in case of longitudinal wave excitation. The scalar potential can be found by using angular spectrum and ray theory techniques. In the following formulae, the superscripts + and - denote the potentials going in the +z and -z directions, respectively and the subscript numbers show the plane of evaluation. Referring to Figure 2.4, following this notation, the spatial scalar potential at the transducer plane,  $u_1^+$ , due to a circular transducer of radius  $a$  generating longitudinal waves, can be written as

$$u_1^+(x, y) = A \text{circ}[(x^2 + y^2)^{1/2}/a] \quad \text{where} \quad \text{circ}(r) = \begin{cases} 1 & r \leq 1 \\ 0 & r > 1 \end{cases} \quad (2.8)$$

The angular spectrum at the same plane,  $U_1^+$ , can be found by Fourier transformation:

$$\begin{aligned} U_1^+(k_x, k_y) &= \mathcal{F}\{u_1^+(x, y)\} = 4a^2 A \text{jinc}[(a/\pi)(k_x^2 + k_y^2)^{1/2}] \\ &= 2\pi a^2 A J_1[a(k_x^2 + k_y^2)^{1/2}]/[a(k_x^2 + k_y^2)^{1/2}] \end{aligned} \quad (2.9)$$

where  $J_1$  is the Bessel function of the first kind and  $k_x$  and  $k_y$  are the  $x$  and  $y$  components of the wavevector,  $\mathbf{k}_1$ , in the lens rod. Since the lens rod has length  $l$ , the angular spectrum at  $z = l$ ,  $U_2^+$ , can be found as

$$U_2^+(k_x, k_y) = 4a^2 A \text{jinc}[(a/\pi)(k_x^2 + k_y^2)^{1/2}] \exp(jk_z l) \quad (2.10)$$

where  $k_z = (k_1^2 - k_x^2 - k_y^2)^{1/2}$ , is the component of  $\mathbf{k}_1$  in the  $z$  direction. The exponential factor,  $\exp(jk_z l)$ , takes care of the plane wave propagation in  $z$  direction, hence the diffraction. Then the spatial distribution,  $u_2^+$ , is found by inverse Fourier transformation:

$$u_2^+(x, y) = \mathcal{F}^{-1}\{U_2^+(k_x, k_y)\} \quad (2.11)$$

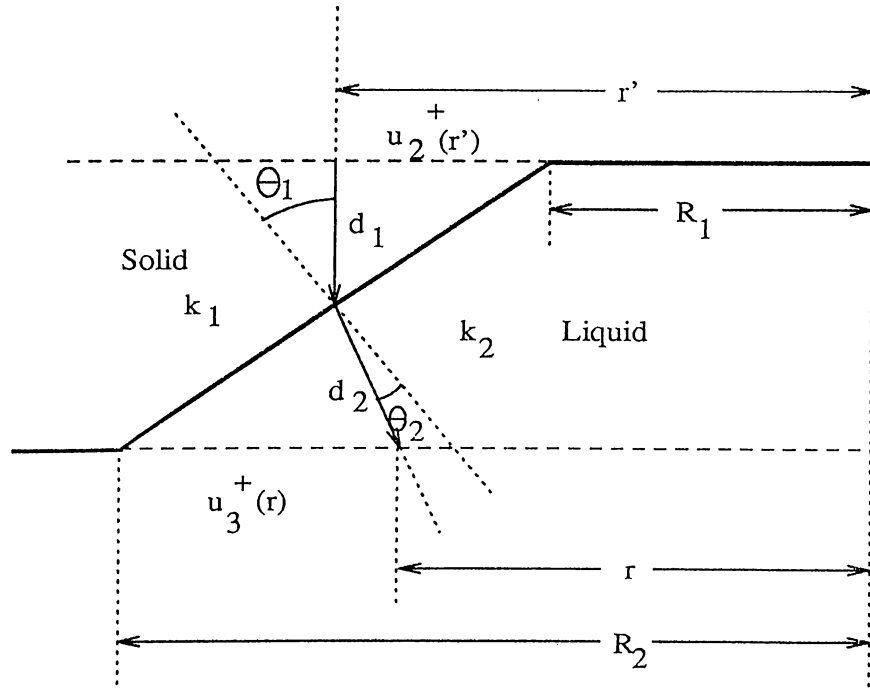


Figure 2.9: Geometry for the Ray Theory.

To find the field distribution at plane 3, ray theory is used. Referring to Figure 2.9, it is seen that, since the center part is blocked, only the field distribution in the region  $R_1 \leq (x^2 + y^2)^{1/2} \leq R_2$ , contributes to the field at plane 3. Using ray theory, keeping the amplitude of the rays constant and changing its phase taking care of the ray paths in the lens rod, the field distribution at the conical surface is found. Then the rays are refracted from the surface according to Snell's Law, the amplitude is scaled by  $A_R$  considering power conservation and the phase is changed taking care of the path in the liquid. So, the spatial field distribution at plane 3,  $u_3^+$ , is found approximately as

$$u_3^+(r) = \begin{cases} (r'/r)^{1/2} A_R u_2^+(r') \exp\{j(k_1 d_1 + k_2 d_2)\} & R_1 < r' < R_2 \\ 0 & \text{elsewhere} \end{cases} \quad (2.12)$$

where  $A_R = (1 + \tan \theta_1 \tan(\theta_1 - \theta_2))^{1/2}$ ,  $r = (x^2 + y^2)^{1/2}$ ,  $r' = (r + R_2 \tan \theta_1 \tan(\theta_1 - \theta_2)) / (1 + \tan \theta_1 \tan(\theta_1 - \theta_2))$ ,  $k_1 \sin \theta_1 = k_2 \sin \theta_2$ , and  $d_1 = (r' - R_1) \tan \theta_1$  and  $d_2 = (R_2 - r') \tan \theta_1 / \cos(\theta_1 - \theta_2)$ . Here  $k_1$  and  $k_2$  are the wavenumbers in the lens rod and the liquid medium, respectively.

To have propagation to the material surface and reflection at the interface, we transform the spatial field distribution,  $u_3^+$ , into angular angular spectrum,  $U_3^+$ , as

$$U_3^+(k_x, k_y) = \mathcal{F}\{u_3^+(x, y)\} \quad (2.13)$$

Then the reflected angular spectrum at plane 3,  $U_3^-$ , is written as

$$U_3^-(k_x, k_y) = U_3^+(k_x, k_y) \exp\{j2k_z'Z\} \mathcal{R}(k_x/k_2, k_y/k_2) \quad (2.14)$$

where  $k_z' = (k_2^2 - k_x^2 - k_y^2)^{1/2}$  and the exponential factor takes care of the propagation distance  $2Z$  in  $z$  direction, since the distance between the lens and the material surface is  $Z$ . The reflection process at the interface is included through the multiplication by the reflection coefficient,  $\mathcal{R}(k_x/k_2, k_y/k_2)$ . The output voltage,  $V$ , at the transducer terminals can be found in terms of incident and reflected angular spectra at plane 3, by the help of an integral formula derived from reciprocity relations as

$$V = -\frac{c_{11}k_2^2}{8\pi^2\omega P} \int_{-\infty}^{+\infty} \int_{-\infty}^{+\infty} k_z' U_3^+(-k_x, -k_y) U_3^-(k_x, k_y) dk_x dk_y \quad (2.15)$$

where  $c_{11}$  is the longitudinal constant of the liquid medium,  $\omega$  is the angular frequency and  $P$  is the incident power at the transducer terminals. Noting that the problem has circular symmetry, the substitution,  $k_r = (k_x^2 + k_y^2)^{1/2}$  can be made where  $k_r$  is the radial wavenumber. Then the output voltage,  $V$ , as a function of frequency,  $f$ , can be written as

$$V(f) = -\frac{c_{11}k_2^2}{4\pi\omega P} \int_0^{+\infty} k_r k_z' U_3^+(k_r) U_3^-(k_r) dk_r \quad (2.16)$$

In the foregoing argument using the ray acoustics approximation, zero field is assumed out of a certain region in plane 3 ignoring the diffraction from the upper and lower edges of the lens. Some error occurs due to this approximation, but since we find the result by integrating the fields, it becomes negligibly small. Also, it should be noted that the frequency response of the transducer is not taken into consideration in the above derivation.

## 2.4 $V(f)$ Curves

As seen in the previous section, the output voltage of the Lamb wave lens can be expressed as a function of the frequency of operation, lens geometry and the reflection coefficient of the layered material. By recording the output signal of the Lamb wave lens while the frequency of excitation is scanned, one obtains a characteristic  $V(f)$  curve, which shows the excited modes as peaks.

The formation of  $V(f)$  curve can be easily explained by transforming the velocity dispersion curves in Figure 2.1 to a critical angle versus frequency curves. For this transformation, a fixed thickness is assumed and the relation



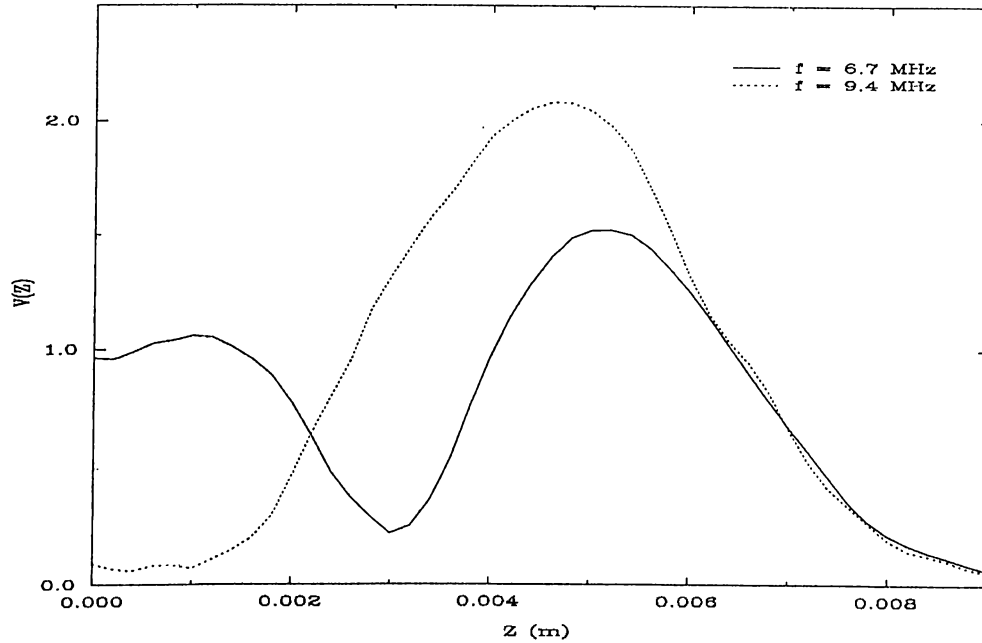


Figure 2.10: The variation of output signal amplitude as a function of lens-sample distance for two different frequency values for the sample in Figure 2.8.

$\theta_c = \sin^{-1}(v_l/v)$  is used to transform the velocity to critical angle, where  $\theta_c$  is the critical incidence angle,  $v_l$  and  $v$  are the velocity of sound in the liquid and velocity of the mode, respectively. After this transform, these curves show the variation of critical angle of the modes with frequency. At frequencies where the critical angle of a leaky mode becomes equal to the fixed incidence angle of the Lamb wave lens, the particular mode is excited resulting in nonspecular reflection. In Figure 2.10, the variation of output signal amplitude as a function a function of the distance between the lens and the layered material is calculated for two frequencies. At  $f = 6.7$  MHz, the critical angle is matched and a leaky mode is excited, so the variation of the field depicted in Figure 2.2 is seen as a peak, a null region and a larger peak. Since the Lamb wave lens is placed close to the material to detect leaky waves, there will be a high output signal due to the first peak. At  $f = 9.4$  MHz, the matching condition is not satisfied, no leaky wave is excited and there is only one peak in  $V(Z)$  curve resulting from the specular reflection, hence the output signal is low. Since many modes can be excited at a fixed incidence angle by scanning the frequency, the  $V(f)$  curve takes the form of shifted peaks each corresponding to a different mode, showing the single mode excitation ability of the Lamb wave lens.

The relation between the reflection coefficient of the material and  $V(f)$

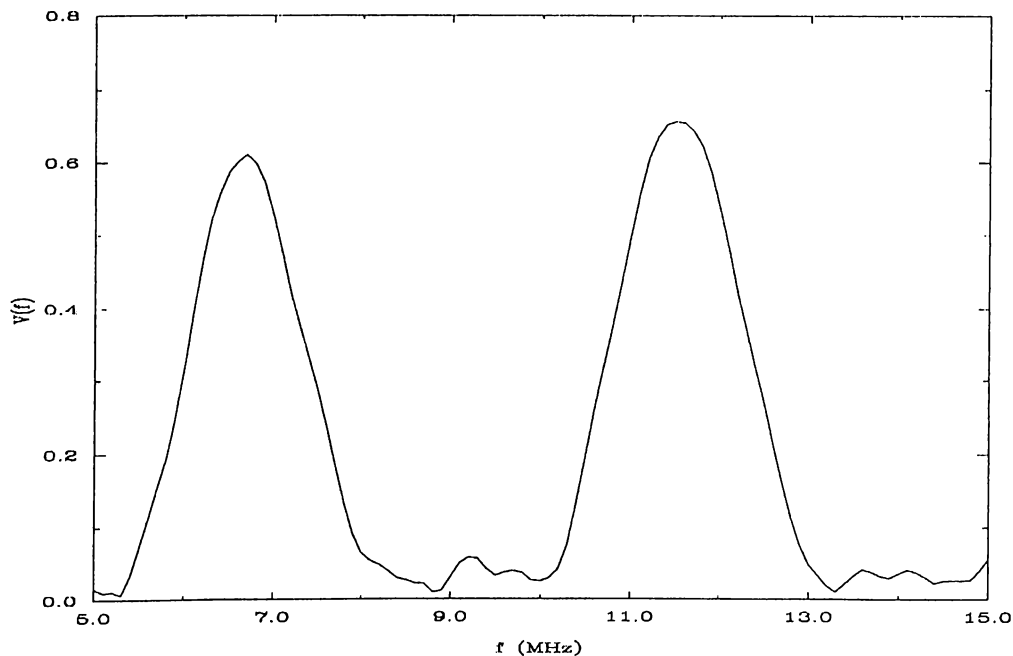


Figure 2.11: The  $V(f)$  curve of the sample in Figure 2.8.

curve can be observed by referring to the Figures 2.8 and 2.11. The peaks of  $V(f)$  curve occur at frequencies where phase transitions are observed in the  $R(f)$  curve, hence the  $V(f)$  curve directly provides the phase, in other words, critical angle information of the reflection coefficient. In fact, in the frequency range of interest, the magnitude of reflection coefficient is unity and all the information is in the phase which is contained in the  $V(f)$  curve.

Since any perturbation of elastic and physical parameters of the layered material such as thickness, density, elastic constants and bond quality at the interface changes the reflection coefficient, a corresponding change in  $V(f)$  is expected. The most drastic change is the shift of the phase transitions in frequency resulting a shift in the peak positions of the  $V(f)$  peaks. The parameter sensitivity of  $V(f)$  is investigated by simulations and the obtained results are presented in Chapter 5.

The bond quality at the interface between the layer and substrate is also effective on the  $V(f)$  curves, since it effects the reflection coefficient through the changes in the boundary conditions. In Figure 2.12, the calculated  $V(f)$  curves of the aluminum layered silicon sample in water for three bond quality conditions are plotted. In good bond case, perfect bonding at the interface is considered. The case when the layer is in contact with, but slips on the substrate is referred as slippery bond and the delaminated bond corresponds to the condition that the layer and substrate are completely separated by an

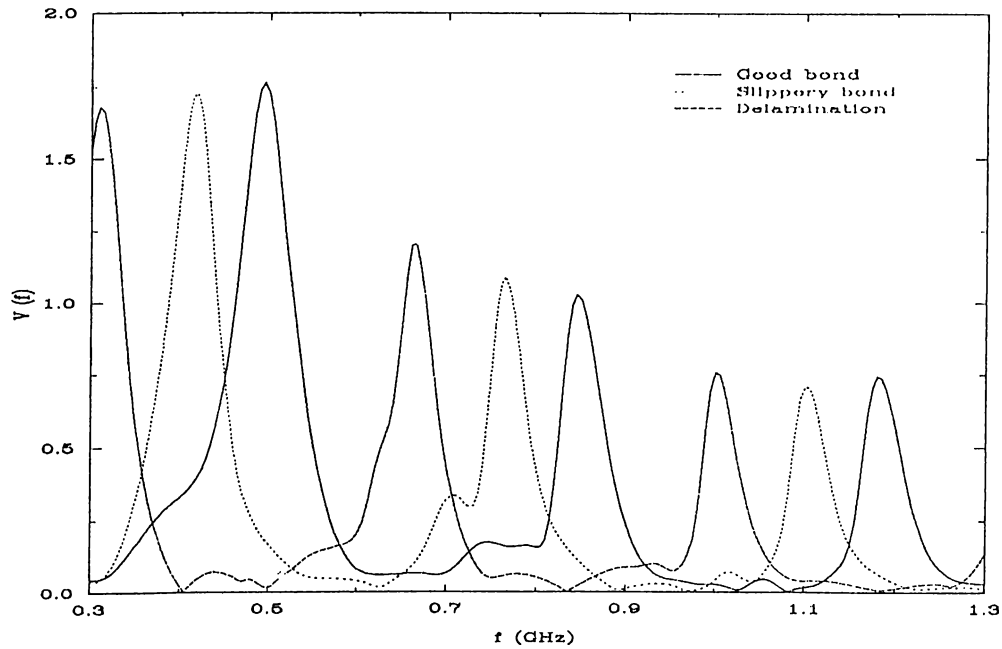


Figure 2.12: Calculated  $V(f)$  curves for a good bond, slippery bond and delamination at the interface of  $6 \mu\text{m}$  aluminum layer on silicon substrate.

other material. In the delamination case in Figure 2.12, air is assumed to exist between the layer and substrate. All three cases are easily differentiated by observing their effects on the  $V(f)$  curve showing a unique ability of the Lamb wave lens. In the simulations, a sapphire lens with  $\theta_1 = 22^\circ$ ,  $\theta = 19^\circ$ ,  $R_1 = 42.5 \mu\text{m}$  and  $R_2 = 250 \mu\text{m}$  is used.

## Chapter 3

### Simulation

In order to compare the theory of the Lamb wave lens with the experiments, a computer program simulating the Lamb wave lens response is developed in C programming language. It mainly consists of calculation of the reflection coefficient and the field propagation and integral calculations involved in the derivation of the  $V(f)$  curve.

#### 3.1 Calculation of the Reflection Coefficient

For the reflection coefficient calculation the layered material is modeled as in Figure 3.1. A solid layer of thickness  $d$  is assumed on a semi-infinite substrate and this structure is overlaid by a semi-infinite fluid. Following the notation in [18], we have a scalar potential function  $\Phi$  and a vector potential  $\Psi$  which correspond to longitudinal and shear wave motion, respectively. Assuming particle motion in  $x - z$  plane, we have  $\Psi = \hat{a}_y \Psi_y$  and  $\Psi_y \equiv \Psi$ . With these potential functions, we have the relations

$$u_x = \frac{\partial \Phi}{\partial x} - \frac{\partial \Psi}{\partial z} \quad (3.1)$$

$$u_z = \frac{\partial \Phi}{\partial z} + \frac{\partial \Psi}{\partial x} \quad (3.2)$$

$$Z_x = \mu \left( 2 \frac{\partial^2 \Phi}{\partial x \partial z} + \frac{\partial^2 \Psi}{\partial x^2} - \frac{\partial^2 \Psi}{\partial z^2} \right) \quad (3.3)$$

$$Z_z = (\lambda + 2\mu) \frac{\partial^2 \Phi}{\partial z^2} + \lambda \frac{\partial^2 \Phi}{\partial x^2} + 2\mu \frac{\partial^2 \Psi}{\partial x \partial z} \quad (3.4)$$

where  $u_x$  and  $u_z$  are the tangential and normal components of the particle displacement and  $Z_x$  and  $Z_z$  are the tangential and normal stresses, respectively

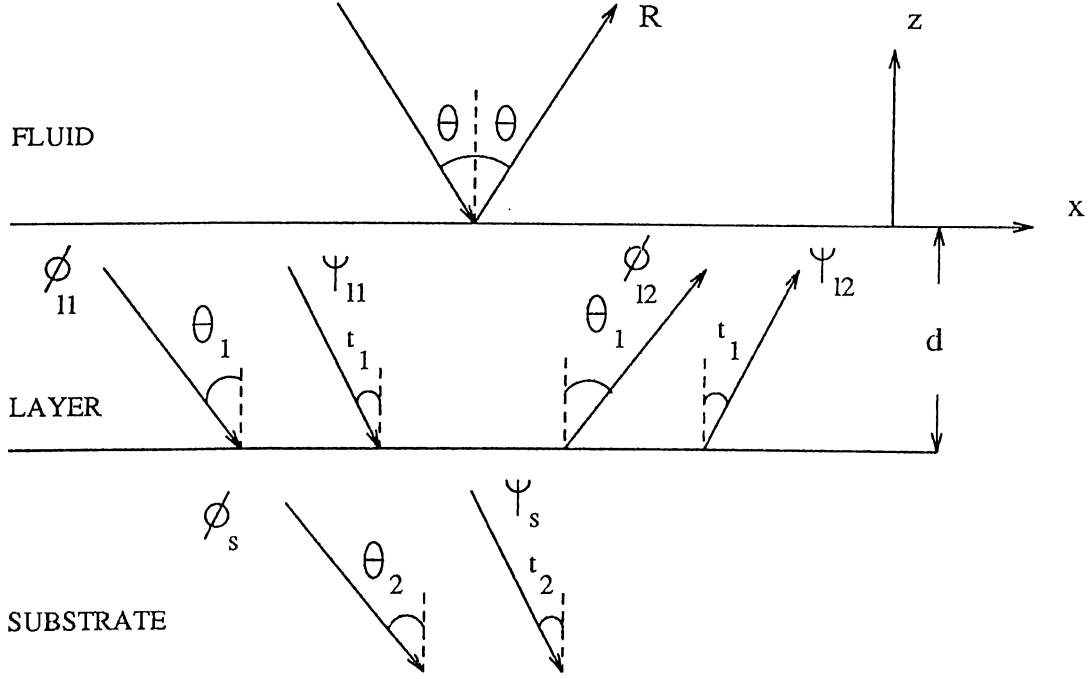


Figure 3.1: Geometry and coordinate system for the layered material.

and  $\lambda$  and  $\mu$  are the Lamé constants related to the longitudinal and shear wave speeds,  $c_l$ ,  $c_s$ , and density,  $\rho$ , as

$$\rho c_l^2 = \lambda + 2\mu, \quad \rho c_s^2 = \mu \quad (3.5)$$

Referring to Figure 3.1, assuming that a plane wave of unit amplitude is incident on the layered material from the fluid medium at angle  $\theta$  we have the wave potentials in the phasor form suppressing harmonic time dependence as

$$\Phi_f = \exp(jk_f x \sin \theta) (\exp(-jk_f z \cos \theta) + R \exp(jk_f z \cos \theta)) \quad (3.6)$$

$$\Phi_l = \exp(jk_l x \sin \theta_1) (\phi_{l1} \exp(-jk_l z \cos \theta_1) + \phi_{l2} \exp(jk_l z \cos \theta_1)) \quad (3.7)$$

$$\Psi_l = \exp(j\kappa_l x \sin t_1) (\psi_{l1} \exp(-j\kappa_l z \cos t_1) + \psi_{l2} \exp(j\kappa_l z \cos t_1)) \quad (3.8)$$

$$\Phi_s = \exp(jk_s x \sin \theta_2) \phi_s \exp(-jk_s z \cos \theta_2) \quad (3.9)$$

$$\Psi_s = \exp(j\kappa_s x \sin t_2) \psi_s \exp(-j\kappa_s z \cos t_2) \quad (3.10)$$

where the subscripts  $f$ ,  $l$  and  $s$  denote the media, 1, 2 denote the incident and reflected fields and  $k$  and  $\kappa$  refer to the longitudinal and shear wave numbers in corresponding media, respectively.

The boundary conditions on the particle displacement and stress are used to obtain a systems of linear equations to solve the unknown potentials [19]. To compare the results for different bonding conditions, three separate programs are written employing appropriate boundary conditions for each case.

In good bonding case, the normal component of particle displacement and both tangential and normal stress are continuous at the fluid-layer interface with zero tangential stress in the fluid medium yielding the equations

$$u_{zf} = u_{zl}, \quad Z_{zf} = Z_{zl}, \quad Z_{xl} = 0 \quad \text{at } z = 0 \quad (3.11)$$

At the layer-substrate interface all the components of the particle displacement and stress are continuous to give the equations

$$u_{xl} = u_{xs}, \quad u_{zl} = u_{zs}, \quad Z_{xl} = Z_{xs}, \quad Z_{zl} = Z_{zs} \quad \text{at } z = -d \quad (3.12)$$

In the case of slippery bonding at the layer-substrate interface, the boundary conditions yielding equations 3.11 remains the same, but since it is assumed that the layer can slip on the substrate in lateral direction, continuity of tangential displacement is not valid, and the tangential stress is zero at the layer-substrate interface. As a result we have same equations in 3.11 and instead of the equations in 3.12, we have

$$u_{zl} = u_{zs}, \quad Z_{zl} = Z_{zs}, \quad Z_{xl} = 0, \quad Z_{xs} = 0 \quad \text{at } z = -d \quad (3.13)$$

The delamination case is approximated by assuming that the layer is a solid plate separating two different fluid media. Referring to the Figure 3.1, it corresponds to a fluid substrate. Since we do not have shear potential in the fluid substrate, i.e.  $\psi_s=0$ , the number of unknowns is 6. Again we have the same equations as in 3.11 and in addition we have the equations

$$u_{zl} = u_{zs}, \quad Z_{zl} = Z_{zs}, \quad Z_{xl} = 0 \quad \text{at } z = -d \quad (3.14)$$

The equations can be written in terms of the unknown potentials by substituting the results of equations 3.6 through 3.10 in the equations 3.1 through 3.4. Since we have equal number of equations and unknowns, the reflection coefficient,  $R$ , in equation 3.6 can be found in each case of bonding. The developed programs evaluate the equations and solve the system of equations for  $R$  using Cramer's rule. The results are in good agreement with the published ones [20][21].

### 3.2 Calculation of $V(f)$ Curves

For the calculation of the  $V(f)$  curves theoretically, the steps explained in the section 2.3 are implemented by a program. Since the problem involves many transformations back and forth between spatial and angular domains, an efficient transformation algorithm should be used.

Since the problem has circular symmetry, the Fourier transform becomes the Hankel transform in cylindrical coordinates. An efficient method called Quasi Fast Hankel Transform (QFHT) [22] is used for the implementation of Hankel transform. A pair of Hankel transform of order 0 is defined as

$$\begin{aligned} g(\rho) &= 2\pi \int_0^{\infty} r f(r) J_0(2\pi \rho r) dr \\ f(r) &= 2\pi \int_0^{\infty} \rho g(\rho) J_0(2\pi \rho r) d\rho \end{aligned} \quad (3.15)$$

For QFHT, first a Gardner Transform variable change is performed

$$r = r_0 \exp(\alpha x), \quad \rho = \rho_0 \exp(\alpha y) \quad (3.16)$$

where  $r_0$ ,  $\rho_0$  and  $\alpha$  are constants to be determined considering some relations to avoid aliasing. With this variable change and defining new functions as

$$\begin{aligned} f(x) &= r f(r) = r_0 \exp(\alpha x) f(r_0 \exp(\alpha x)) \\ g(y) &= \rho f(\rho) = \rho_0 \exp(\alpha y) g(\rho_0 \exp(\alpha y)) \\ j(x + y) &= 2\pi \alpha r_0 \rho_0 \exp(x + y) J_0(2\pi \alpha r_0 \rho_0 \exp(x + y)) \end{aligned} \quad (3.17)$$

the Hankel transform integrals in Eq. 3.15 become

$$\begin{aligned} g(y) &= \int_{-\infty}^{\infty} f(x) j(x + y) dx \\ f(x) &= \int_{-\infty}^{\infty} g(y) j(x + y) dy \end{aligned} \quad (3.18)$$

It is observed that the transform integrals are converted into cross-correlation integrals, which can be efficiently evaluated by Fast Fourier Transform (FFT) methods. To apply FFT methods, the functions in Eq. 3.18 are converted to discrete sequences of length  $N$ , then a discrete approximation to the Hankel transform integrals is written as

$$\begin{aligned} g[m] &= \sum_{n=0}^{N-1} f[n] j[n + m] \\ f[n] &= \sum_{m=0}^{N-1} g[m] j[n + m] \end{aligned} \quad (3.19)$$

To have correct results, the  $N$ -point sequences are extended into  $2N$ -point sequences by padding with zeros from  $m, n = N$  to  $2N - 1$ . Then the summations in Eq. 3.19 become  $2N$ -point circular convolutions. The criteria for choosing the parameters  $r_0$ ,  $\rho_0$  and  $\alpha$ , considering aliasing, becomes

$$N = K_2 \beta b \ln(K_1 \beta b), \quad \alpha \exp(\alpha N) = K_1 / K_2, \quad r_0 \rho_0 = (K_2 / K_1^2) \alpha \quad (3.20)$$

where  $\beta$  is the highest spatial frequency and  $b$  is the largest radial distance. We have the relations  $r_0 = 1/K_1 \beta$  and  $\Delta \rho_N = 1/K_2 b$ , so the condition  $K_1, K_2 \geq 2$  should be satisfied to avoid aliasing. Once  $N$ ,  $K_1$  and  $K_2$  are determined, the other parameters can be found using the relations in Eq. 3.20. Using QFHT, for each Hankel transform,  $2N \log_2(4N)$  complex multiplications and additions are performed, whereas  $N^2$  complex multiplications and additions are required for direct evaluation of the integrals by trapezoid approximation with the same accuracy.

$N$  is chosen as 4096 for the calculations, and for each lens with different frequency range and dimensions, the other parameters are found satisfying the required conditions. The error resulting from the discrete approximation in Eq. 3.19 is calculated and it is seen to be negligibly small. For each frequency value, 3 QFHT's are performed and the field propagation is included by complex multiplications.

In  $V(f)$  calculations, the acoustic attenuation in the fluid and the effect of anisotropic lens rod material on diffraction loss are also considered for correct simulation. The acoustic attenuation in fluid is included in two parts. First, referring to Figure 2.4, each ray reaching plane 3 after refraction from the conical recess, is attenuated depending on the length of its path in the fluid. Then, after finding the angular spectrum at plane 3, each plane wave component is attenuated considering the propagation between the lens and the material surface. The effect of the anisotropic lens rod material on diffraction loss is included by calculating the equivalent diffraction length of the lens rod,  $l'$ , using the relation  $l' = l(1 - 2b)$ , where  $l$  is the physical length of the lens rod and  $b$  is the anisotropy factor [23].

After finding the field distributions at material surface, the voltage integral is evaluated by trapezoid approximation. In this evaluation, at every sampling point, the reflection coefficient at the corresponding incidence angle is calculated and multiplied with the field distributions. The result is then normalized by the proper constants to give the final voltage value.



## Chapter 4

### Experimentation

An experimental setup is implemented and some specially prepared layered samples are used to test the theory of the Lamb wave lens and its ability to characterize and image the layered materials. The functional diagram of the setup is given in Figure 4.1. The setup mainly consists of the Lamb wave lens, electronics to excite the lens properly, scanning system for imaging and a PC for data acquisition and control.

#### 4.1 The Lens

A Lamb wave lens is designed and fabricated for experimental purposes. The lens rod is made of aluminum. Referring to fig 2.4, its length,  $l$ , is 5.9 cm. The conical recess has an upper radius,  $R_1=3.1$  mm and a lower radius,  $R_2=5.95$  mm. The angle of the cone is chosen to be as  $\theta_1 = 45.5^\circ$  resulting conical waves incident to the layered material with an incidence angle,  $\theta = 35.8^\circ$  from water after refraction from aluminum-water interface. The center part is blocked by acoustic absorbant to prevent direct reflection from this region.

An air-backed PZT-5H piezoelectric ceramic transducer is used for acoustic wave generation. It has a radius,  $a=8.5$  mm and it is bonded to the lens rod by phenyl salicylate. The transducer has a resonance frequency of 7 MHz with a 3 dB bandwidth of 3.4 MHz, limiting the useful band of the setup to 5–9 MHz. With this bandwidth, at most two leaky modes can be excited in the prepared samples with layer thickness in the range 0.4–0.7 mm to obtain a  $V(f)$  curve, since at most critical angles of two modes can be matched to the angle of the lens in this frequency range.

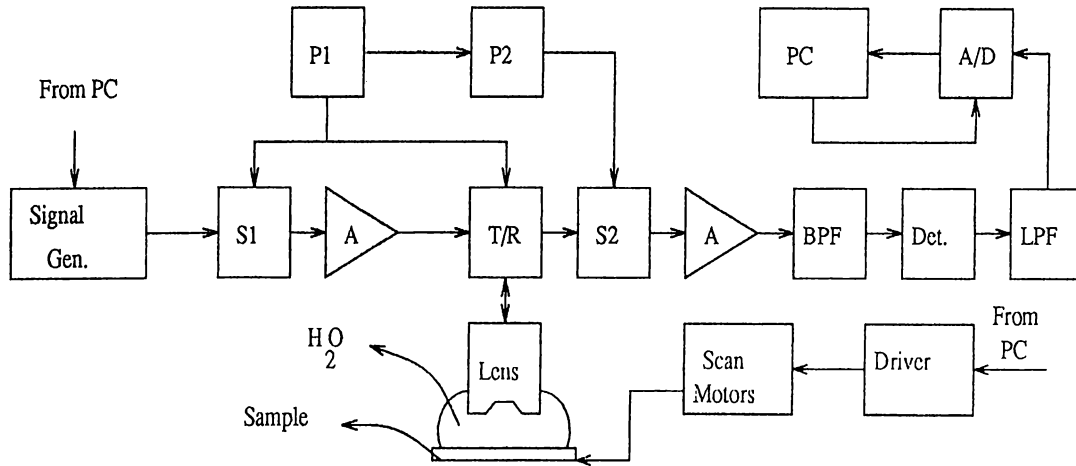


Figure 4.1: Functional block diagram of the experimental setup.

## 4.2 Electronic Setup

The electronic system is operated in the 5–9 MHz frequency band due to the limitation imposed by the transducer, although the components have a larger bandwidth. Referring to Figure 4.1, the sine wave of desired frequency generated by the computer controlled signal generator is time gated by the switch S1, which is in turn controlled by the pulser P1. The sine burst is amplified and sent to the transducer through the T/R switch, which is also controlled by P1. The width of the pulse generated by P1 should be at least 4-5 cycles long to resemble continuous wave excitation and reduce the band of the signal, but it should be short enough to avoid interference. 800 ns is found to be a proper pulse width for P1. The repetition rate should be high to increase the signal to noise ratio but it should be low enough such that the transducer response will decay in one period. A compromise is found at 800 Hz.

The return signal is passed from T/R switch to switch S1, controlled by pulser P2, which generates a pulse with an adjustable width and delay with respect to P1. The delay between P1 and P2 is adjusted considering the propagation time of the acoustic waves in the lens, liquid and the material to detect only the desired signal reflected from the sample. The signal is then amplified and passed through a 5-10 MHz band pass filter for noise reduction. A negative detector is used to extract the envelope of the signal. The detector output is passed through a low pass filter to get its dc part and amplified before A/D conversion controlled by the computer. For point  $V(f)$  measurements, the output of the band pass filter is recorded from the scope while changing the frequency.

### 4.3 Imaging Setup

The return signal of the Lamb wave lens can also be used for imaging. If the sample under test is scanned mechanically, while recording the amplitude of return signal at a fixed frequency at every pixel, an amplitude image (AI) of the sample can be obtained. High contrast AI's, showing the spatial variation of material parameters, bond quality and subsurface defects in the sample, can be recorded if the frequency is properly adjusted.

In our imaging setup, the sample is placed in a water-filled tank mounted on a surface which can be mechanically scanned. Two identical stepper motors are used to move the sample in the  $X - Y$  plane in raster fashion. The motors have maximum speed of 250 steps/sec. with a step size of  $10 \mu\text{m}$ . They are driven by a driver unit controlled by the computer (Figure 4.1). During the imaging process, the computer moves the sample and at every imaging point, it performs an A/D conversion, then stores the pixel value in the memory. The PASCAL program is written to perform the above operations. With the present setup, AI of a  $2 \text{ cm}^2$  area is taken in nearly 15 minutes with 200 points in each direction. The mechanical speed is the limiting factor, with faster motors this duration can be reduced.

As pointed out in section 2.4, the shift in the peak frequency of a particular mode is the most significant result in  $V(f)$ , when a change occurs in the parameters of the material or bond quality at the interface. So, a peak frequency image (PFI), formed by mapping the peak frequency of a particular mode in the  $V(f)$  curve, can directly provide information about the related local properties of the layered material.

For PFI, at every imaging point the frequency is scanned in a range, i.e.  $V(f)$  is recorded, and the peak frequency is found by detecting and comparing the return signal at every frequency step. Then the peak frequency value is stored as data of that pixel. A computer program, which scans both the sample mechanically and the frequency electronically synchronously with data acquisition is written. The frequency scan is done by controlling the signal generator using IEEE 488 Standard. For this purpose, an IEEE 488 interface card is installed in the PC and operated by a program in BASIC. A PFI of a  $2 \text{ cm}^2$  area is taken in the order of hours with 0.1 MHz frequency steps and 0.1 mm step size in both directions. The speed is limited by mechanical reasons and the scan speed of the signal generator.

## 4.4 The Samples

In order to investigate the characterization and imaging ability of the Lamb wave lens, some layered materials are specially prepared as samples. Considering the geometry and frequency band of the fabricated lens, some layer-substrate pairs are found to be suitable for investigation by the help of the simulation program. Among them, copper layer on steel substrate is seen to be feasible to prepare.

Copper layer is deposited onto steel by electroplating. It is known that to have a strong bond between the deposited layer and steel substrate, the substrate should be processed in copper cyanide solution prior to the regular plating process in copper sulphate solution [24]. This fact is used to produce well defined regions of poor bond at the interface. After cleaning the surface, the areas at which poor bond is desired are masked and the substrate is plated in copper cyanide solution. Then, the mask is removed and the plating is continued in copper sulphate solution. The samples are plated to a thickness of 0.7 mm and then surface ground to required levels. Since the layer thickness should be in the order of wavelengths, the layer thickness was kept in the 0.4 - 0.65 mm range. The samples show no optical indication of different bond regions.

## Chapter 5

### Results

In this chapter, simulated and experimental  $V(f)$  curves are presented and compared. The amplitude and peak frequency images of a sample are presented.

#### 5.1 $V(f)$ Results

The theory of the Lamb wave lens is checked by comparing the theoretical  $V(f)$  curves computed by the simulation program with the experimental  $V(f)$  curves measured on the prepared samples by the setup explained in Chapter 4. Especially the effect of bond quality on  $V(f)$  is investigated. In the comparisons, both the experimental and simulation results are normalized considering the frequency response of the transducer. In Figure 5.1, the calculated and measured  $V(f)$  curves of a sample with 0.6 mm copper layer on steel substrate are compared. In simulations three bonding conditions are considered. The  $V(f)$  measurements are done at two spots. One is at a good bond region and the other is at a point where a poor bond is induced. The comparison shows that the poor bond is a slippery bond. In Figure 5.2, a similar comparison is made for another sample with 0.5 mm copper layer. In this case, it is seen that the poor bond is a delamination with air separating the layer and the substrate. In both cases good agreement is observed between the computed and measured curves.

The parameter sensitivity of  $V(f)$  is investigated by simulations performed on an 6  $\mu\text{m}$  aluminum layered silicon substrate sample. As seen in Figure 5.3, the  $V(f)$  is very sensitive to changes in the density,  $\rho$ , and the shear constant,  $c_{44}$ . In the simulations, a sapphire lens operating in 0.8–1.3 GHz frequency

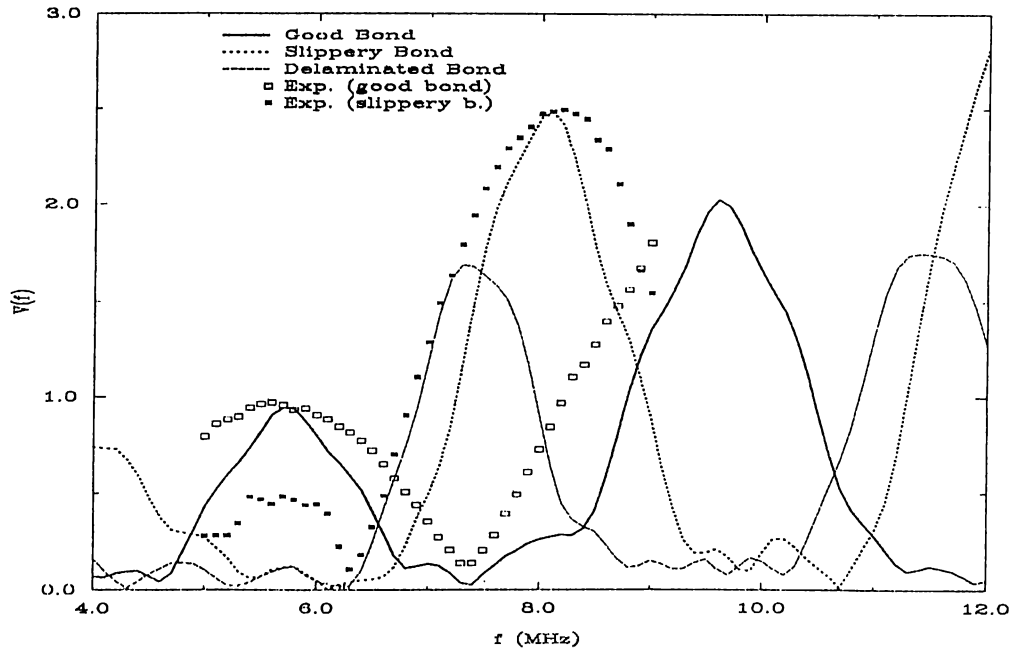


Figure 5.1: Calculated and measured  $V(f)$  curves for a good bond and slippery bond. The sample is 0.6 mm copper layered steel substrate.

band with  $\theta = 19^\circ$ ,  $R_1 = 45 \mu\text{m}$ ,  $R_2 = 300 \mu\text{m}$  is used. The percent shift in the peak frequency of  $V(f)$  curve of a particular mode as function of percent changes in the shear constant,  $c_{44}$ , and the density,  $\rho$ , of the layer material is plotted in Figure 5.4. It is seen that for small perturbations, the relation is almost linear. It is also observed that the effect of  $c_{11}$  of the layer and the parameters of the substrate have negligible effect on  $V(f)$  peaks. The shear wave velocity of the layer is the most effective parameter on  $V(f)$  curves.

In all the layered materials considered above, the layer has softer acoustic properties than the substrate. This case is referred in the literature as “loaded” substrate. To show the application of  $V(f)$  technique to the opposite case, which is called “stiffened” substrate, simulations are also done on chromium layered steel substrate. This kind of layered materials support only the Rayleigh-like mode [20]. In Figure 5.5, the calculated  $V(f)$  curves of 40  $\mu\text{m}$  chromium layered steel are plotted for good bond, slippery bond and delamination cases. The simulations are done assuming a lens made of glass operating in 20–40 MHz frequency band, with  $\theta = 31.8^\circ$ ,  $R_1 = 0.98 \text{ mm}$ , and  $R_2 = 2.64 \text{ mm}$ . A peak is observed in the frequency range of interest for slippery bond and delamination, in contrast to the low signal level for good bond case, showing that the Lamb wave lens can also be used to differentiate bond quality in stiffened substrates.

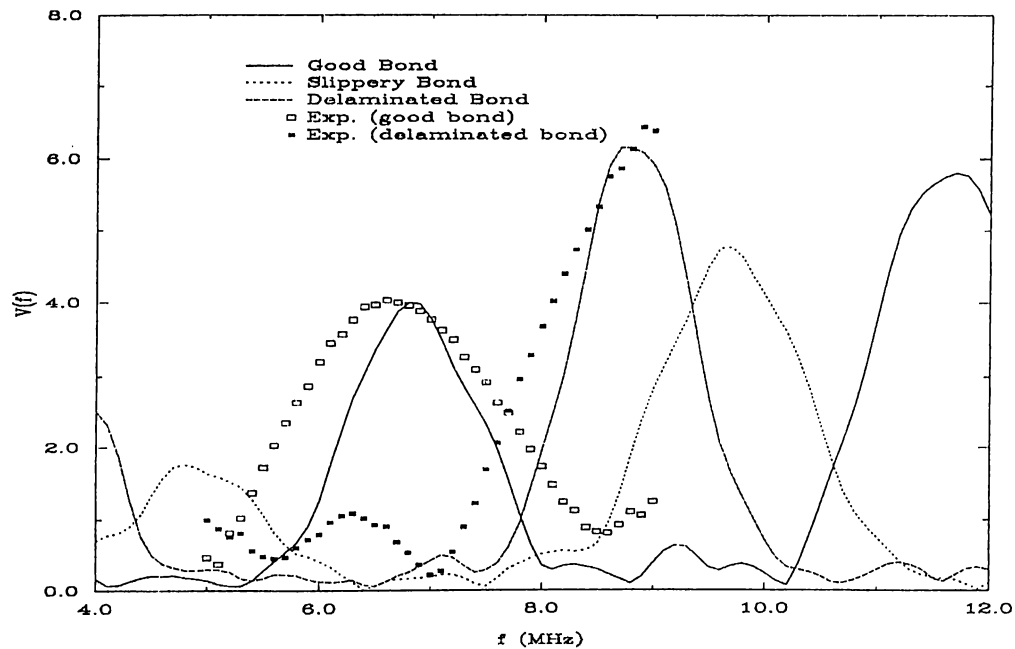


Figure 5.2: Calculated and measured  $V(f)$  curves for a good bond and a delamination. The sample is 0.5 mm copper layered steel substrate.

## 5.2 Images

The spectral shape of the  $V(f)$  curve is determined by the reflection coefficient of the layered material at that point. Since the reflection coefficient is highly dependent on the bond quality at the layer-substrate interface,  $V(f)$  directly provides bond quality information. Part of this information can be exploited by obtaining amplitude images as explained in section 4.3. If the frequency of excitation is chosen such that the amplitude difference between different types of bond is maximized, the resulting image will indicate the regions of different bond quality successfully. For the sample in Figure 5.1, 7.9 MHz was chosen as the frequency of excitation for amplitude imaging, providing maximum amplitude difference between slippery and good bond regions. Figure 5.6 shows the amplitude image of a 2 cm by 2 cm region of the sample described in Figure 5.1. The induced slippery region is a 1 cm by 1 cm square, and it is clearly identified. It should be noted that the regions with different bond quality are not differentiable optically.

As seen in Figure 5.1, the frequency of the peak in  $V(f)$  due to a particular mode shifts from 9.7 MHz in case of good bond, to 8.1 MHz in the case of slippery bonding at the interface. Hence a peak frequency image (PFI) can be formed as explained in section 4.3 to differentiate the bond quality. For

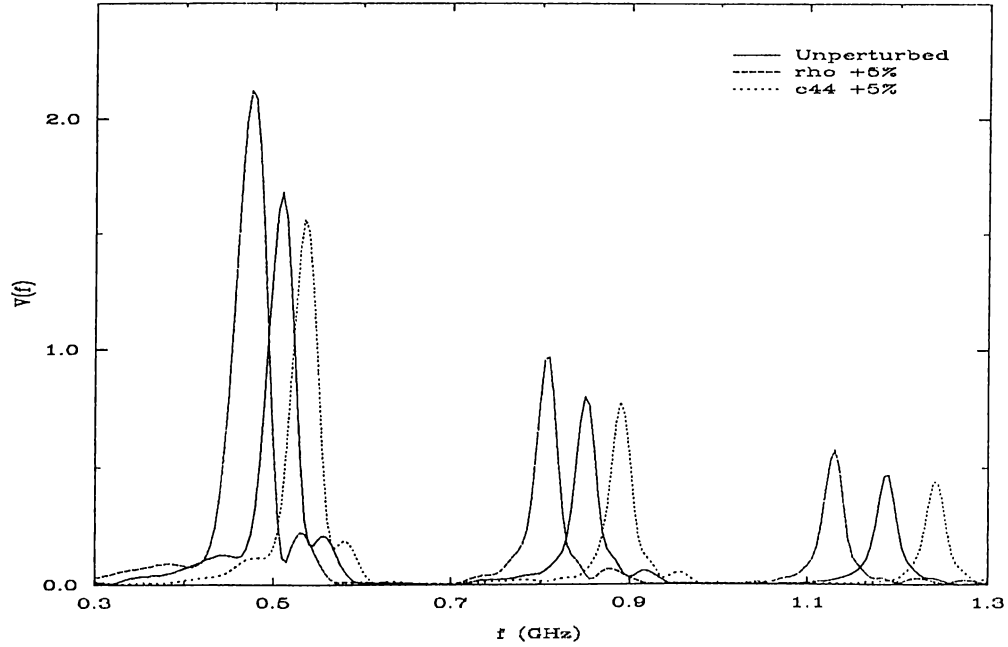


Figure 5.3: Calculated  $V(f)$  curves for unperturbed, and perturbed layer parameters in case of good bond. The density,  $\rho$ , and shear constant,  $c_{44}$ , of the layer are increased 5 %.

the sample in Figure 5.1, at every imaging point, the local peak frequency around 8 MHz is found and a PFI is formed by plotting the peak frequency as a function of position. The obtained PFI of the same region in Figure 5.6 is shown in Figure 5.7. The regions with high intensity indicate higher peak frequencies, i.e. the regions with good bond at the interface, and the dark region caused by lower peak frequencies, shows the induced poor bond. Again the square shaped poor bond region is identified and the peak frequency is constant in that region.

The axial resolution of the images is equal to the layer thickness since the Lamb wave modes propagate predominantly in the layer. The lateral resolution is not very easy to define since any perturbation in the region that is insonified by the lens disturbs the return signal, but the effect of the focal region is the most significant. It should be noted that no sign of these bond differences at the interface is visible optically on the surface of the samples.



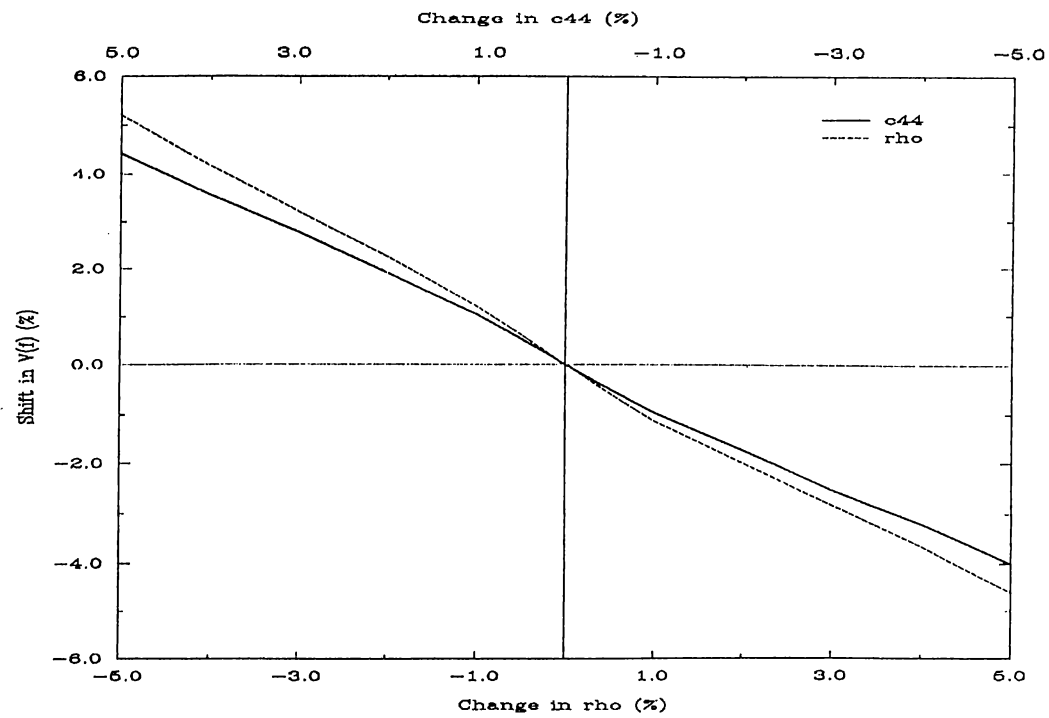


Figure 5.4: Calculated percentage shift in  $V(f)$  as a function of percentage changes in layer  $\rho$  and  $c_{44}$ .

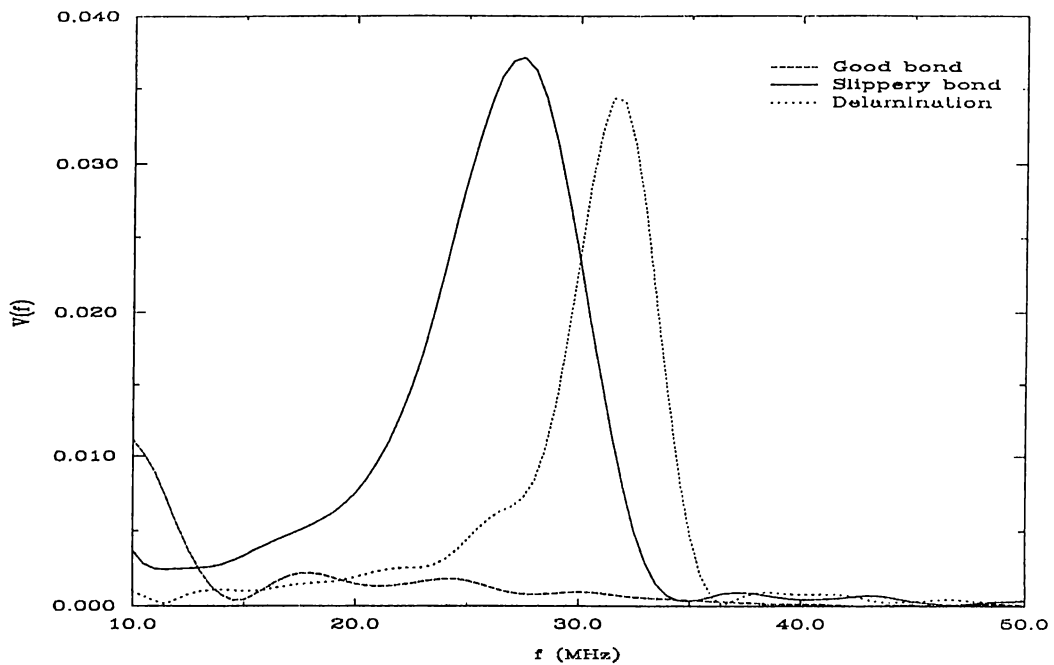


Figure 5.5: Calculated  $V(f)$  curves for good bond, slippery bond and delamination for  $40 \mu\text{m}$  chromium layer on steel substrate.

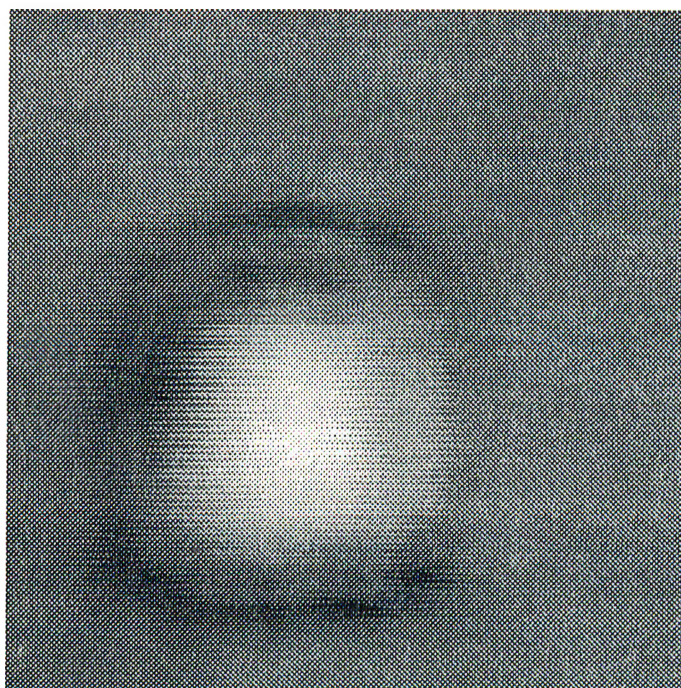


Figure 5.6: Amplitude image of the sample with 0.6 mm Cu layer on steel at 7.9 MHz.

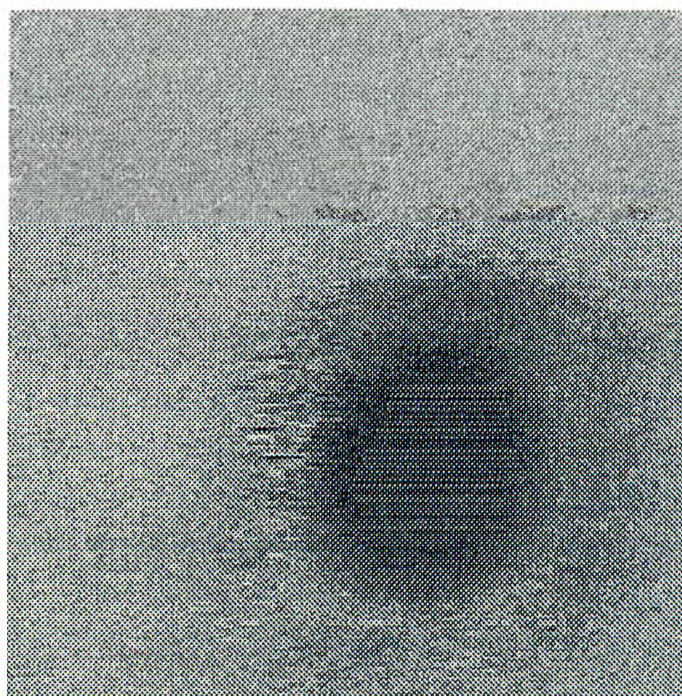


Figure 5.7: Peak frequency image of the same region in Figure 5.6.

## Chapter 6

### Conclusion

The Lamb wave lens can be used as a lens of acoustic microscopes for quantitative characterization and imaging of layered materials. The unique  $V(f)$  curve of the layered material, obtained by a simple frequency scan, emerges as a new characterization method providing plenty of information about the elastic and physical parameters of the material and the bond quality at the interface. The good agreement seen between the experimental and theoretical results show that the technique can be used to make sensitive parameter measurements.

In the  $V(f)$  measurements, the main mechanical accuracy requirement is the alignment of the samples with the lens to have right angle for detection of reflected waves. The Lamb wave lens does not have a critical focusing problem of the spherical lens, as long as it does not receive specular reflections, the distance to the material surface does not alter the output signal significantly. As a system requirement, a system using the Lamb wave lens should be able to scan the operation frequency to excite different modes because of the fixed incidence angle. Also, to investigate different layered materials, Lamb wave lenses with different incidence angles may be required.

The Lamb wave lens can easily identify bonding problems in layered materials. It can differentiate the nature of some bonding problems at the interfaces, which is by other means very difficult. Images of such interfaces can either be made in the form of an amplitude image or a PFI. For amplitude imaging, the frequency should be properly adjusted so as to have maximum contrast. As compared to amplitude images, PFI images contain more information and are safer to interpret.

The Lamb wave lens, which becomes a powerful tool for layered material

characterization and imaging, seems to have a promising future with applications to multilayered materials, anisotropy and attenuation measurements.

## Appendix A

### Calculation of the curvature matrix of a cone

For a curved surface  $z = f(x, y)$  with  $z$ -axis normal to the surface at the point  $P$  where  $x = y = z = 0$ , the curvature matrix of the surface at  $P$  in the directions of  $x$  and  $y$  axes is defined as

$$\mathbf{C} = \begin{bmatrix} f_{xx} & f_{xy} \\ f_{xy} & f_{yy} \end{bmatrix} \quad (\text{A.1})$$

where  $f_{xx} = \partial^2 f / \partial x^2$  etc. are evaluated at  $x = y = 0$ .

Let us consider a cone in rectangular coordinates as in Figure A.1 with half angle  $\alpha$ . Then the formula of the cone can be written as

$$x^2 = \cot^2 \alpha (z^2 + y^2) \quad (\text{A.2})$$

where  $\cot \alpha = c/a$ . Suppose that we want to find the curvature matrix at an arbitrary point  $P$  as shown in Figure A.1. To have  $z$ -axis normal to the surface of the cone the  $x$  and  $z$  axes are rotated by  $\alpha$  degrees counterclockwise resulting in the primed coordinates as

$$x = z' \sin \alpha + x' \cos \alpha, \quad z = z' \cos \alpha - x' \sin \alpha, \quad y = y' \quad (\text{A.3})$$

Eq. A.2, after some manipulations, can be written in primed coordinates as

$$z'^2 - x'z' \tan 2\alpha + y'^2 \left( \frac{\cos^2 \alpha}{\cos 2\alpha} \right) = 0 \quad (\text{A.4})$$

To have  $x'' = y'' = z'' = 0$  at point  $P_0$ , the  $x'$ -axis is shifted by an amount  $x_0$  to yield new coordinates

$$x'' = x' - x_0, \quad z'' = z', \quad y'' = y' \quad (\text{A.5})$$

Then Eq. A.4 becomes

$$z''^2 - (x'' + x_0)z'' \tan 2\alpha + y''^2 \left( \frac{\cos^2 \alpha}{\cos 2\alpha} \right) = 0 \quad (\text{A.6})$$

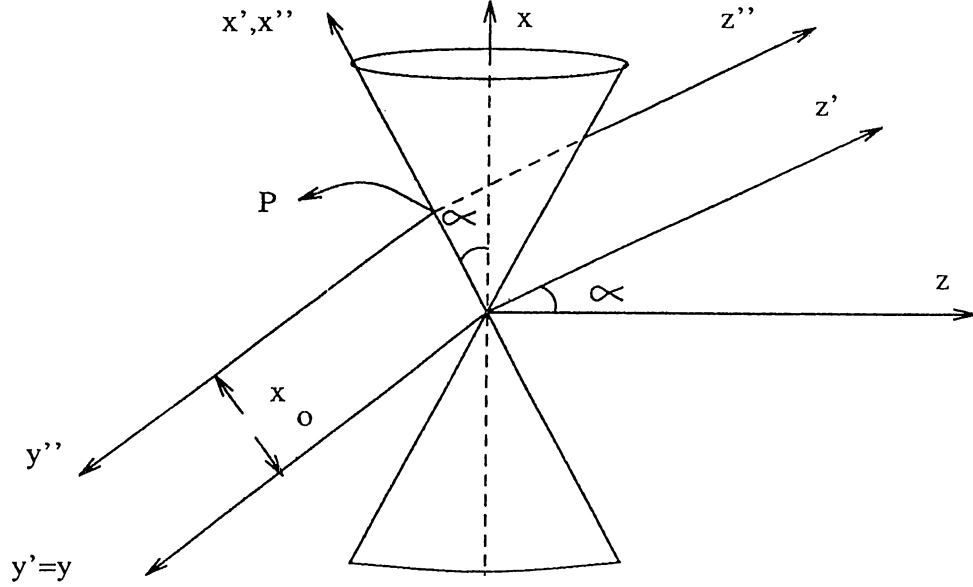


Figure A.1: Geometry and the coordinate system of the cone.

To have the equation of the surface in the form  $z'' = f(x'', y'')$ ,  $z''$  is solved from Eq. A.6. The roots of Eq. A.6 can be found as

$$z''_{1,2} = \frac{1}{2} \{ (x'' + x_0) \tan 2\alpha \mp \sqrt{\Delta} \} \quad (\text{A.7})$$

where  $\Delta = (x'' + x_0)^2 \tan^2 2\alpha - 4y''^2 (\cos^2 \alpha / \cos 2\alpha)$ . The root with positive sign is taken to have a convex surface.

To find the curvature matrix, the derivatives,  $f_{x''x''}$ ,  $f_{x''y''}$  and  $f_{y''y''}$  are found and evaluated at  $x'' = y'' = z'' = 0$  resulting

$$f_{x''x''} = f_{x''y''} = 0 \quad (\text{A.8})$$

$$f_{y''y''} = -\frac{4 \cos^2 \alpha}{x_0 \sin 2\alpha} \quad (\text{A.9})$$

Thus, the curvature matrix,  $C$ , of the cone at point  $P$  is found as

$$C = \begin{bmatrix} 0 & 0 \\ 0 & -\frac{4 \cos^2 \alpha}{x_0 \sin 2\alpha} \end{bmatrix} = \begin{bmatrix} \frac{1}{R_{x''}} & 0 \\ 0 & \frac{1}{R_{y''}} \end{bmatrix} \quad (\text{A.10})$$

where  $R_{x''}$  and  $R_{y''}$  are the radii of curvature in the directions of the  $x''$  and  $y''$  axes, respectively.

## Appendix B

### Material Constants Used in Simulations

In this appendix, the longitudinal acoustic wave velocity,  $V_l$ , shear acoustic wave velocity,  $V_s$ , and density,  $\rho$ , of the materials used in the simulations are tabulated.

Material	$V_l(m/sec)$	$V_s(m/sec)$	$\rho(g/cm^3)$
Air	344		$1.24 \times 10^{-3}$
Aluminum	6420	3040	2.7
Chromium	6650	4030	7.0
Copper	5010	2270	8.93
Glass (Pyrex)	5640	3280	2.24
Sapphire	11100	6040	3.99
Silicon	11000	6250	3.27
Steel	5900	3200	7.9
Water	1509		1.0

## References

- [1] R. B. Thompson and D. O. Thompson, "Ultrasonics in nondestructive evaluation," *Proc. IEEE*, vol. 73, pp. 1716-1755, December 1985.
- [2] C. F. Quate, A. Atalar and H. K. Wickramasinge, "Acoustic microscopy with mechanical scanning-a review," *Proc. IEEE*, vol. 67, pp. 1092-1114, 1979.
- [3] A. Atalar, "An angular spectrum approach to contrast in reflection acoustic microscopy," *J. Appl. Phys.*, vol. 49, pp. 5130-5139, 1978.
- [4] K. K. Liang, G. S. Kino and B. T. Khuri-Yakub, "Material characterization by inversion of  $V(Z)$ ," *IEEE Trans. Sonics Ultrason.*, vol. 32, pp. 213-224, 1985.
- [5] A. Atalar and H. Köymen, "A high efficiency Lamb wave lens for subsurface imaging," in *Proc. IEEE 1989 Ultrasonics Symposium*, pp. 813-816, 1989.
- [6] A. Atalar, H. Köymen and L. Değertekin, "Characterization of layered materials by the Lamb wave lens," in *Proc. IEEE 1990 Ultrasonics Symposium*, pp. 359-363, 1990.
- [7] A. Atalar, L. Değertekin and H. Köymen, "Acoustic parameter mapping of layered materials using a Lamb wave lens," *Acoustical Imaging*, vol. 19, 1991.
- [8] G. W. Adler and E. L. Farnell, "Elastic wave propagation in thin layers," in *Physical Acoustics*, W. P. Mason and R. N. Thurston, eds., vol. 9, pp. 35-127, Academic, 1972.
- [9] D. E. Chimenti, A. H. Nayfeh, "Leaky Lamb waves in fibrous composite laminates," *J. Appl. Phys.*, vol. 58, pp. 4531-4538.
- [10] H. L. Bertoni and T. Tamir, "Unified theory of Rayleigh-angle phenomena for acoustic beams at liquid-solid interfaces," *Appl. Phys.*, vol. 2, pp. 157-172, 1973.



- [11] D. E. Chimenti, A. H. Nayfeh, D. L. Butler, "Leaky Rayleigh waves on a layered halfspace," *J. Appl. Phys.*, vol. 53, pp. 170-176, 1982.
- [12] L. E. Pitts, T. J. Plona and W. G. Mayer, "Theory of nonspecular reflection effects for an ultrasonic beam incident on a solid plate in a liquid," *IEEE Trans. Sonics Ultrason.*, vol. 24, pp. 101-108, 1977.
- [13] H. L. Bertoni and T. Tamir, "Characteristics of wedge transducers for acoustic surface waves," *IEEE Trans. Sonics Ultrason.*, vol. 22, pp. 415-420, 1975.
- [14] H. Köymen and A. Atalar, "Focussing surface waves using axicons," *Appl. Phys. Lett.*, vol. 47, p. 1266, 1985.
- [15] A. Atalar and H. Köymen, "Use of a conical axicon as a surface acoustic wave focusing device," *IEEE Trans. Ultrason. Ferro. and Freq. Cont.*, vol. 34, pp. 53-63, 1987.
- [16] G. A. Deschamps, "Ray Techniques in electromagnetics," *Proc. IEEE*, vol. 60, pp. 1022-1035, 1972.
- [17] A. Atalar, "A backscattering formula for acoustic transducers," *J. Appl. Phys.*, vol. 51, pp. 3093-3098, 1980.
- [18] L. M. Brekhovskikh, "Waves in layered media", 2.ed., Academic, New York, 1980.
- [19] D. B. Bogy and S. M. Gracewski, "On the plane wave reflection coefficient and nonspecular reflection of bounded beams for layered half-spaces underwater," *J. Acoust. Soc. Am.*, vol. 74, pp. 591-599, 1983.
- [20] A. H. Nayfeh, D. E. Chimenti, "Reflection of finite acoustic beams from loaded and stiffened halfspaces," *J. Acoust. Soc. Am.*, vol. 75, pp. 1360-1368, 1984.
- [21] T. J. Plona, L. E. Pitts and W. G. Mayer, "Ultrasonic bounded beam reflection and transmission effects at a liquid/solid-plate/liquid interface," *J. Acoust. Soc. Am.*, vol. 59, pp. 1324-1328, 1976.
- [22] A. E. Siegman, "Quasi fast Hankel transform," *Optics Letters*, vol. 1, p. 13, 1977.
- [23] A. Atalar, "A fast method of calculating diffraction loss between two facing transducers," *IEEE Trans. Ultrason. Ferro. and Freq. Cont.*, vol. 35, pp. 612-617, 1988.

- [24] F. A. Lowerheim, "Electroplating," *Kirk-Othmer Encyclopedia of Chemical Technology*, 3. ed., vol. 8, pp. 826-869, 1979.